Ocean Engineering 365 (2026) 127077

Contents lists available at ScienceDirect

Ocean Engineering

journal homepage: www.elsevier.com/locate/oceaneng

Research paper

From fin dynamics to navigation control: A simplified framework for batoid-inspired underwater locomotion

Tommaso Scudeletti *, Giovanni Bianchi, Stefano Arrigoni, Simone Cinquemani, Francesco Braghin

Politecnico di Milano, Dipartimento di Meccanica, Via La Masa 1, Milano, 20156, Italy

ARTICLE INFO

Keywords:
Autonomous underwater vehicle (AUV)
Bioinspired underwater robot
Flexible pectoral fins
Model-free control
6-DOF motion control
Open-water experiments

ABSTRACT

This work presents a simplified and control-oriented framework enabling closed-loop navigation of an underwater robot inspired by a cownose ray and propelled by flexible pectoral fins. This study provides novel fully onboard, open-water demonstrations of closed-loop 6-DOF motion control for a batoid-inspired AUV driven by flexible fins, without external tracking systems: attitude and depth are regulated continuously from onboard sensing, while planar position is corrected intermittently from GPS fixes acquired during resurfacing. A reduced set of kinematic variables is identified to map fin actuation to body forces and moments, allowing the fins to be treated as generalized thrusters without relying on complex hydrodynamic modeling. This abstraction guides the design of a cascaded control architecture integrating quaternion-based attitude regulation, depth control, and absolute heading control. The approach is implemented on a ray-inspired robot equipped with a ROS2-based modular software stack and a lightweight sensor suite. Open water experiments demonstrate reliable orientation control, dynamic reference tracking, helical trajectory execution, and preliminary waypoint navigation, achieving attitude-maintenance RMSE (Root Mean Square Error) of 1.3°–4.4° across yaw/pitch/roll and depth-tracking RMSE of 0.073 m in helical motion. The results show that a control architecture independent of a dynamic model, with control variables related to fin kinematics, provides an effective methodology for autonomous underwater navigation with soft, bioinspired AUVs.

1. Introduction

The demand for silent, efficient, and non-intrusive propulsion technologies continues to grow as interest in underwater robotics increases towards ecological monitoring, infrastructure inspection, human–robot interactions, and stock monitoring in fish farms. Conventional propeller-driven Autonomous Underwater Vehicles (AUVs), despite decades of development and highly mature 6-DOF control architectures, still suffer from well-known drawbacks: mechanical noise, flow disturbance, safety concerns in cluttered environments, and reduced efficiency at low speeds (Picardi et al., 2020; Railey, 2018; Yuan et al., 2024-04-22).

Bioinspired propulsion offers an attractive alternative. The swimming strategies of fish are classified into two groups: Body and/or Caudal Fin (BCF) propulsion and Median and/or Paired Fin (MPF) propulsion (Webb, 1988; Sfakiotakis et al., 1999). BCF swimming involves the propagation of a traveling wave from head to tail that pushes water backwards, and propels the fish for momentum conservation (Salazar et al., 2018). Most MPF swimmers exploit the same physical principle; however, their bodies remain undeformed, and they generate a traveling wave on a pair of appendages. Batoid fishes belong to this last category and use their large pectoral fins for propulsion. Their locomotion strategy, known as rajiform swimming, can be classified into undulatory and oscillatory. Species that live near the seabed and swim in closed environments, like the bluespotted ray, use undulatory swimming, as the wavelength of the traveling wave on their fins is shorter than their body length. This gives them excellent agility in maneuvers in benthic environments, allowing them to curve with a null curvature radius and even swim backwards. On the other side, the oscillatory species, like the giant manta ray, move their fins with a wavelength longer than their body, generating a movement similar to a heaving and pitching hydrofoil, and their swimming strategy is characterized by high energy efficiency and high cruising speed, making them experts in swimming for long distances in pelagic environments (Fish et al., 2016). This classification is not a neat distinction, but there is a continuous range of species, from completely undulating to completely oscillating, with several species able to adapt their locomotion strategy according

* Corresponding author.
E-mail addresses: tommaso.scudeletti@polimi.it (T. Scudeletti), giovanni.bianchi@polimi.it (G. Bianchi), stefano.arrigoni@polimi.it (S. Arrigoni), simone.cinquemani@polimi.it (S. Cinquemani), francesco.braghin@polimi.it (F. Braghin).

https://doi.org/10.1016/j.oceaneng.2026.127077
Received 19 December 2025; Received in revised form 5 July 2026; Accepted 14 July 2026
Available online 29 July 2026

to their needs. The species that lie in the middle of this range, like the cownose ray, provide a good trade-off between energy efficiency and agile maneuvering, and are a promising source of inspiration for bioinspired swimming robots (Rosenberger, 2001).

Several previous studies on ray-inspired robots have focused on hydrodynamics, the development of effective fin actuation mechanisms, and the analysis of the forces generated in relation to fin kinematics and vortices in the wake. These studies have demonstrated that passive fin flexibility is a fundamental feature for efficient bioinspired propulsion and have reproduced the real pectoral fin deformation using different strategies. The first prototype of a ray-inspired robot was developed by Cai et al. who used two flexible membranes as pectoral fins and described the relationship between flapping frequency and generated torque (Cai et al., 2010). Low et al. developed a robot capable of forward swimming, yawing, and gliding with three servomotors per fin (Low et al., 2011). Instead, Ma et al. reproduced the fin deformation by combining chordwise flapping and fin twisting, characterizing the robot swimming speed at different frequencies (Ma et al., 2015). Chew et al. performed a similar study on their manta ray robot, studying also the influence of fin thickness on thrust generation and swimming speed (Chew et al., 2015). Cai et al. built a manta robot with three articulated mechanisms reproducing fin deformation that is capable of highly maneuverable turns and rolling maneuvers (Cai et al., 2019). Another example is the robot developed by Xing et al. which has two motors for each pectoral fin and can faithfully reproduce the eight-shape trajectory of rays' fin tips (Xing et al., 2022), demonstrating that chordwise and spanwise flexibility enhance thrust generation. With another robot, Chen et al. showed that a flexible silicone-rubber fin can reproduce the real fin deformation and propel the robot at a higher speed than a more rigid fin Chen et al. (2022). Bianchi et al. adopted passive, flexible fins and developed a robot capable of 3D locomotion, characterizing its swimming performance across different parameters of fin flapping (Bianchi et al., 2023b). Similarly, Lu et al. showed that pectoral fin flexibility improves propulsion (Lu et al., 2024), whereas Liu et al. analyzed the thrust generation mechanism of a flexible fin and studied how an intermittent gliding–flapping locomotion improves energy efficiency (Liu et al., 2025). He et al. developed a ray-inspired robot whose propulsion is achieved through the sinusoidal actuation of three kinematic links designed to replicate the manta fin motion (He et al., 2025). Asada et al. built a ray robot with three rigid links per fin and analyzed the swimming speed, turning radius, and angular velocity for different kinematic parameters of fin movement (Asada et al., 2025). Zhang et al. developed a robot inspired by a ray with flexible fins actuated by two motors per fin, optimizing the stiffness distribution on the fin thanks to a dynamic model (Zhang et al., 2026).

Other works focused not only on robot design but also on implementing a control algorithm. For example, Zhang et al. developed a Central Pattern Generator (CPG) to maintain the desired phase shift between servomotor and reproduce correctly the traveling wave on the fin, obtaining a robust controller for forward swimming and yawing maneuvers (Zhang et al., 2018). Hao et al. combined a CPG oscillator to move the fin with a higher-level controller that modulates amplitude and phase to adjust the swimming direction, and to control heading to perform pitching and yawing maneuvers (Hao et al., 2022). Another application of CPG-based control on ray-inspired robots is presented by Cao et al. who combined CPG and intermittent flapping–gliding movement to control their robot (Cao et al., 2023). Similar results were obtained with the robot developed by He et al. who adopted an S-plane control for heading and depth in a swimming pool (He et al., 2022). Meng et al. developed an advanced sliding-mode fuzzy controller that relies on an external motion-capture system, enabling complete control of the robot's 3D movement in a swimming pool (Meng et al., 2024). Finally, Zhang et al. developed a combination of fuzzy control and CPG, enabling their robot to adjust its attitude, reach a depth of 30 m, change its heading according to a predetermined reference, and resurface (Zhang et al., 2022). Overall, prior work on batoid-inspired robots can be grouped into:

- studies that focus on the fin design and its hydrodynamics, primarily quantifying thrust generation and efficiency under prescribed actuator movements;
- implementation of low-level controllers, e.g., CPG-based, that regulate fin-wave generation and enable basic maneuvers such as forward swimming and turning;
- implementation of closed-loop controllers either limited to 2D or to controlled pools and/or relying on external tracking hardware.

These robots have demonstrated that rajiform swimming is an effective strategy to propel underwater with great efficiency, agility, and maneuverability. However, robust onboard navigation control architectures comparable to those of thruster-propelled AUVs have not been explored for flexible-finned systems, limiting autonomous operation in real open-water environments.

Conventional thruster-propelled AUVs typically achieve autonomy through a layered, fully onboard navigation architecture. This architecture includes state estimation, cascaded stabilization of attitude, depth, and speed, outer-loop guidance for target following, and control allocation to actuators. In contrast, most ray-inspired prototypes primarily emphasize gait or CPG generation and basic maneuvers. When closed-loop navigation is demonstrated, it is often restricted to controlled environments such as pools or relies on external tracking systems. As a result, autonomy in these systems remains limited by drift and sensitivity to disturbances due to the absence of robust inner control loops, as well as by unpredictable control behavior arising from underactuation and speed-dependent dynamics of flexible fins.

This work addresses this gap by implementing closed-loop navigation control for a batoid robot, enabling it to reach targets in open-water conditions while relying entirely on onboard sensing. Table 1 summarizes these differences with respect to existing flexible-fin control approaches. For this purpose, a previously developed robot (Bianchi and Cinquemani, 2022; Bianchi et al., 2023b) was upgraded, integrating sensors for state estimation and including a modular software based on ROS2. The main novel contributions are:

- a control-oriented abstraction that maps fin actuation to a minimal set of kinematic variables with experimentally repeatable effects, enabling fin-propelled locomotion to be controlled through a compact "generalized thruster" interface without detailed hydrodynamic identification;
- a cascaded, fully onboard 6-DOF control architecture combining quaternion-based attitude regulation, depth control, and absolute-heading planar guidance tailored to flexible fins;
- open-water experimental validation including attitude stabilization, rotating-reference tracking, helical trajectories with depth modulation, and preliminary GPS-assisted multi-target navigation.

The remainder of the article is structured as follows. Section 2 presents the robot's upgraded hardware and software design. Section 3 introduces the simplified dynamic model for propulsion, considering the actuation of the soft pectoral fins and the rigid caudal fins to derive the kinematic variables for locomotion. Section 4 presents the state-estimation framework along with the proposed low-level control architecture and introduces the higher-level controller for full navigation. Section 5 reports the experiments conducted to validate the different parts of the controller. Section 6 discusses the results, and Section 7 provides concluding remarks.

2. Hardware

This study is carried out on a previously developed prototype (Bianchi and Cinquemani, 2022; Bianchi et al., 2023b), but several improvements were performed to include the hardware necessary for navigation control. The robot has a rigid central body, made of an aluminum frame, a box containing all the electronics, and a 3D-printed

Table 1
Comparison of control approaches for flexible-finned batoid-inspired underwater robots. All entries use flexible pectoral fins; the proposed framework is the only one demonstrating fully onboard 6-DOF closed-loop regulation and navigation in open water without external tracking.

Work	Control structure	Regulated DOFs	Feedback/sensing	Validation environment
Zhang et al. (2018)	CPG (traveling-wave phase regulation)	Forward speed; yaw	Open-loop CPG (onboard)	Laboratory (n.r.[a])
Hao et al. (2022)	CPG + amplitude/phase modulation	Heading (yaw); pitch	Onboard	Laboratory (n.r.[a])
Cao et al. (2023)	CPG + flapping–gliding switching (online optimization)	Forward; gliding (depth via gliding)	Onboard	Laboratory (n.r.[a])
He et al. (2022)	S-plane control	Heading; depth	Onboard	Swimming pool
Meng et al. (2024)	Sliding-mode fuzzy	3D path following	External motion-capture	Swimming pool
Zhang et al. (2022)	Thruster + CPG	Attitude; depth; heading	Onboard	Controlled dive (to 30 m)
This work	Cascaded, model-independent	Full 6-DOF	Fully onboard (IMU, pressure, GPS); no external tracking	Open water (field)

[a] n.r.: validation environment not reported as an open-water/field deployment.

Table 2
Sensors used on the robot.

Sensor	Type
MPU-9250	9-axis IMU + magnetometer
MS5837-02BA	Depth/pressure sensor (2 bar)
GT-U7	GPS receiver module
RPi Cam Mod 3 x2	12 MP HDR autofocus camera

shell, whereas the fins are made of silicone rubber and actuated through an aluminum rod embedded in the leading edge and connected to a servomotor (Bianchi and Cinquemani, 2022; Bianchi et al., 2023b). The improvements affected only the rigid central body of the robot, whereas the flexible fins remained unchanged from the previous version. Each fin is made of silicone rubber, and it encompasses a rigid bar in the leading edge, which is actuated by a servomotor. The elastic properties of the silicone rubber fin ensure that this movement results in a traveling wave across the fin surface, recreating the undulatory motion used by cownose rays to propel. To enhance controllability in maneuvers, two caudal fins are installed, acting as rudders (Bianchi et al., 2023b).

The changes made to the previous prototype include enhancements to the main computer, the addition of sensors for state estimation, and adjustments to the geometry to make room for the added components. A reliable estimate of the robot's position and velocity is required for accurate underwater motion control, and there are various available techniques and associated sensors that have been extensively studied in the literature (Fogh Sørensen et al., 2025). The adopted configuration prioritizes simplicity and feasibility given the constraints imposed by the robot's size and cruising speed, and is described in Table 2.

The orientation is estimated using an Inertial Measurement Unit (IMU), specifically the MPU9250, which integrates a three-axis gyroscope, accelerometer, and magnetometer to provide full 9-DOF orientation data. This allows for accurate attitude estimation even during dynamic motion. Depth measurements are obtained from a Blue Robotics MS5837-02BA pressure sensor, which provides high-resolution absolute pressure readings.

Global positioning is obtained via a GT-U7 GPS receiver equipped with a standard active antenna, which provides position fixes during resurfacing events. This inexpensive solution was selected primarily because of the space constraints within the robot.

The robot's electronic board was upgraded to a Raspberry Pi 5 to adopt ROS2 as the primary software framework, enabling higher modularity, scalability, and faster development. This middleware allows the full software to be developed into single task-specific programs that communicate through standardized interfaces (Macenski et al., 2023; Portugal et al., 2024; Macenski et al., 2022).

The integration of this new onboard computer required the addition of a DC–DC converter to stabilize the 2S LiPo battery output and provide a regulated 5 V supply for the computer and sensors (see Fig. 1).

Finally, a re-design of the external structure was necessary to compensate for the increased payload, improving buoyancy and ensuring stability during navigation. The dimensions of the robot are 340 mm, 605 mm, and 85 mm in the X (longitudinal) - Y (lateral) - Z (vertical) directions, respectively, and its mass is 2.47 kg.

The final CAD model of the upgraded robot is shown in Fig. 2, and the final result is shown in Fig. 3.

3. Robot dynamics

Understanding the dynamics resulting from the movement of flexible pectoral fins is challenging due to the strong coupling among fin deformation, added mass effects, fluid–structure interaction, and body motion. While detailed hydrodynamic models exist in the literature (Bianchi et al., 2021), their complexity and parameter uncertainty make them unsuitable for real-time control of the movement during maneuvers.

For these reasons, the objective of this section is not to derive a full physical model of the robot, but to identify a minimal set of kinematic variables that:

1. capture the dominant relationships between fin motion and body forces;
2. exhibit consistent, repeatable effects in experiments;
3. enable the fins to be treated analogously to generalized thrusters in a 6-DOF control architecture
4. characterize the primary disturbances induced by the actuation

Thus, the dynamical model presented here is not used as a predictive simulator of the robot's motion, but rather serves as a guide for structuring the low-level controllers.

3.1. Kinematic description of pectoral fin actuation

Each pectoral fin is driven through a rigid leading edge actuated by a servo motor, while the compliant silicon membrane produces a traveling wave across the surface (Bianchi et al., 2023b). In order to achieve this traveling wave motion, the fin needs to be actuated in a sinusoidal manner, so the fin angle $\alpha_i(t)$ $(i = 1, 2)$ can be expressed as

$$\alpha_i = A_i \sin(\omega_i t) + \alpha_{ui} ,$$

where A_i is the oscillation amplitude, ω is the common fin oscillation frequency, and α_{ui} is a static offset angle.

The average thrust over one period generated by each fin is primarily a function of amplitude and frequency, while the direction of the thrust depends on the offset angle (Chew et al., 2015; Bianchi et al., 2023b). At the low forward velocities of this robot, the relative

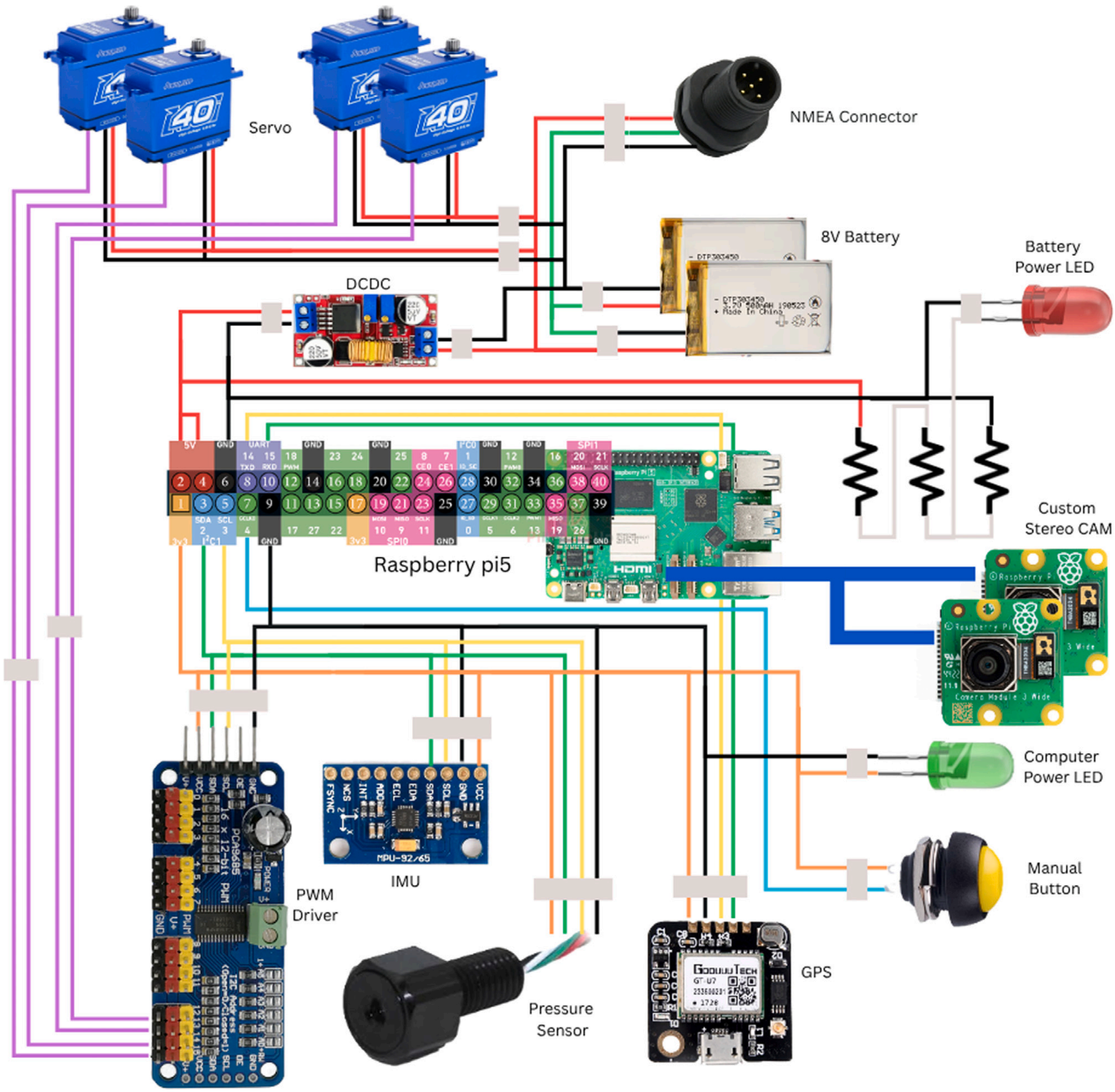

Fig. 1. Onboard electronics schematic.

flow along the fin chord is relatively small, allowing a quasi-steady approximation in which the force generated by the fins is independent of the forward speed, so they depend predominantly on fin kinematic variables.

3.2. Qualitative analysis of the forces acting on pectoral and caudal fins

The forces generated by each fin are evaluated independently, transferred to the main body through joint force balance, and transported to the robot's center of mass. The combination of the force and moment contributions of each fin yields the influence of each actuator on the robot's six DOFs.

The forces acting on each fin are shown in Fig. 4, and they are separated into hydrodynamic forces, i.e., the propelling force and resistive drag, and inertial forces, originating from the acceleration and rotation of the fin mass and its added mass.

The hydrodynamic force $f_i(A_i, \omega)$ is aligned with the wave propagation direction, which combines a chordwise and a spanwise traveling wave, resulting in a direction rotated by an angle Ψ from the perpendicular to the leading edge. This force can be projected on the axes of the robot's reference system, obtaining: a dominant thrust component $f_{x,i}$ aligned with the longitudinal axis (X); a component $f_{yz,i}$, which is modulated by the offset angle α_{ui} and can be decomposed into a lateral component $f_{y,i}$, and a vertical component $f_{z,i}$. The projection of the force f_i on the direction perpendicular to the leading edge of the pectoral fin is called $f_{l,i}$.

Similarly, the contribution of inertial forces can be divided into centrifugal forces $F_{c,i}$ function of the joint angular velocity $\dot{\alpha}_i^2$, tangential inertial forces $F_{I,i}$, and inertial torque $T_{I,i}$ directly resulting from the joint's angular acceleration $\ddot{\alpha}_i$, as shown in Fig. 4(b).

The caudal fins behave predominantly as control surfaces, much like standard rudders. So when rotated by angles θ_i $(i = 1, 2)$, they generate hydrodynamic drag forces, dependent on the angle θ_i, that can be considered orthogonal to their chord. Inertial terms due to $\dot{\theta}_i$ and $\ddot{\theta}_i$ are included in the analysis and divided into the same contribution as for the pectoral fins, obtaining the forces presented in Fig. 5.

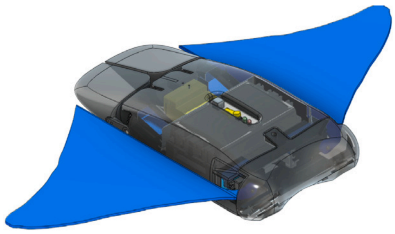

(a) Perspective view of the robot

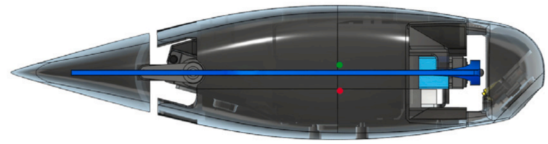

(b) Right view of the robot: in red the Center of mass and in green the center of buoyancy

(c) top view of the robot: in red the Center of mass

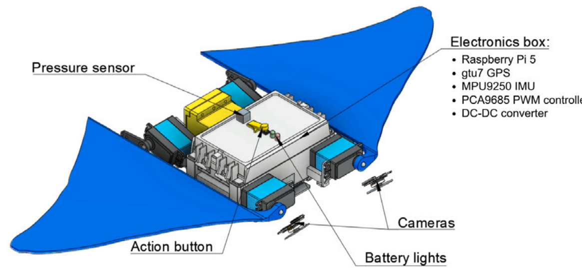

(d) Position of the hardware in the robot

Fig. 2. CAD model of the robot. Dimensions: [Width: 600 mm (185 mm without fins), Length 340 mm, Height 85 mm].

Fig. 3. The assembled robot "Maui".

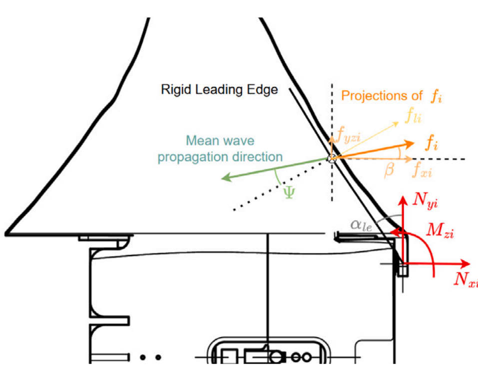

(a) Forces on the XY plane

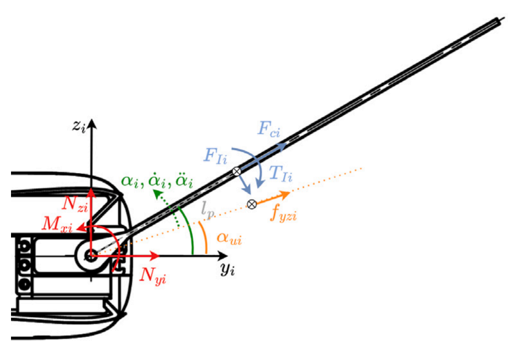

(b) Forces on the YZ plane

Fig. 4. Forces on a single pectoral fin.

3.3. Control-oriented kinematic variables

The qualitative analysis is formalized by expressing all fin-generated forces in a common reference frame and evaluating their resulting forces and torques about the robot's center of mass, as shown in Fig. 6.

The complete derivation, reported in Appendix, proceeds in three steps: first, the constraint forces and moments at each fin joint are expressed as functions of the kinematic variables

A_i, ω, α_{ui} *and* θ_i

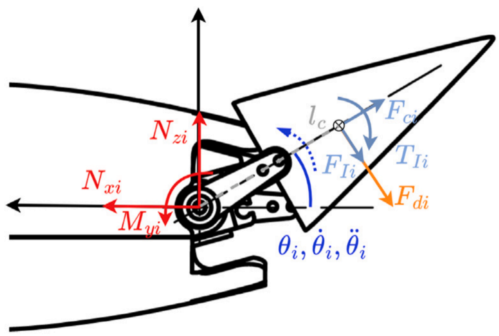

Fig. 5. Forces on a single caudal fin in the XZ plane.

trough dynamic equilibrium equations (Appendices A.1 and A.4); then, these quantities are transported to the robot's center of mass through a rigid-body force and moment balance (Appendices A.2 and A.5); and, finally, the resulting expressions are simplified assuming that the forces generated with the fluid are much greater than the inertial forces, valid at the low forward velocities of this platform, and by treating the inertial terms as bounded periodic disturbances. It is important to note that the reference system of each pectoral and caudal fin are oriented having their X-axis aligned with the forward direction, and their Y-axis pointing outward, resulting in opposite orientation of their Z-axes and meaning that an upward movement of a fin on the left side corresponds to a positive rotation (α_1, θ_1) and an upward movement of a fin on the right side corresponds to a negative rotation (α_2, θ_2). In Equations from (1) to (6), a reduced formulation is presented that isolates the hydrodynamic contributions relevant to controller development, while the inertial terms are treated as disturbances induced by this type of actuation. The terms colored in blue are the forces dependent on the pectoral fin oscillation amplitude, the terms colored in orange express the dependency of these forces on the mean angle of the pectoral fins, the terms in teal express the dependency on the caudal fin angles, and finally, the terms in black are constants. From these expressions, the symmetric properties of the robot emerge, and it is possible to understand how to exploit them to find input parameters useful for control design.

$$F_{hydro,x} = f_x(A_1,\omega) + f_x(A_2,\omega) - K_d(\dot{x})\left[\sin^2\theta_1 + \sin^2\theta_2\right] \tag{1}$$

$$F_{hydro,y} = f_{yz}(A_1,\omega)\cos(\alpha_{u1}) - f_{yz}(A_2,\omega)\cos(\alpha_{u2}) \tag{2}$$

$$\begin{aligned} F_{hydro,z} = {} & f_{yz}(A_1,\omega)\sin(\alpha_{u1}) - f_{yz}(A_2,\omega)\sin(\alpha_{u2}) \\ & - K_d(\dot{x})\left[\sin\theta_1\cos\theta_1 - \sin\theta_2\cos\theta_2\right] \end{aligned} \tag{3}$$

$$\begin{aligned} T_{hydro,x} = {} & a_p\left[f_{yz}(A_1,\omega)\sin(\alpha_{u1}) + f_{yz}(A_2,\omega)\sin(\alpha_{u2})\right] \\ & - a_c K_d(\dot{x})\left[\sin\theta_1\cos\theta_1 + \sin\theta_2\cos\theta_2\right] \end{aligned} \tag{4}$$

$$\begin{aligned} T_{hydro,y} = {} & -b_p\left[f_{yz}(A_1,\omega)\sin(\alpha_{u1}) - f_{yz}(A_2,\omega)\sin(\alpha_{u2})\right] \\ & - b_c K_d(\dot{x})\left[\sin\theta_1\left(\cos\theta_1 + \frac{l_c}{b_c}\right) - \sin\theta_2\left(\cos\theta_2 + \frac{l_c}{b_c}\right)\right] \end{aligned} \tag{5}$$

$$\begin{aligned} T_{hydro,z} = {} & d_{le}\left[f_{le}(A_1,\omega) - f_{le}(A_2,\omega)\right] + a_p\left[f_x(A_1,\omega) - f_x(A_2,\omega)\right] \\ & + K_d(\dot{x})\left[\sin^2\theta_1 - \sin^2\theta_2\right] \end{aligned} \tag{6}$$

As shown in Eq. (1), an equal oscillation amplitude ($A_1 = A_2$) leads to the generation of forward thrust F_x. Conversely, a differential oscillation amplitude ($A_1 \neq A_2$) causes a yawing torque T_z and a lateral force F_y, as shown in Eqs. (2) and (6). An equal mean rotation on the two pectoral fins ($\alpha_1 = -\alpha_2$) is responsible for a pitching moment T_y and a vertical force F_z, as shown in Eqs. (3) and (5). Instead, a different mean rotation ($\alpha_1 \neq -\alpha_2$) generates a rolling torque T_x, as shown in Eq. (4). The effect of the caudal fins is present only when the robot is already swimming, since they act as rudders that deflect the incoming water flow, and for any angle other than zero of either fin, a resistive force is generated along the longitudinal direction X. Moreover, when the two caudal fins have an equal rotation ($\theta_1 = -\theta_2$), a vertical force F_z, and a pitching moment T_y are generated, whereas, when they are different ($\theta_1 \neq -\theta_2$), a rolling and a yawing moment are generated.

Table 3
Control-oriented kinematic parameters.

Symbol	Meaning
A_m	Mean oscillation amplitude
A_d	Difference in oscillation amplitude
α_m	Mean offset angle of pectoral fins
α_d	Difference between offset angles of pectoral fins
θ_m	Mean angle on caudal fins
θ_d	Difference between angles of caudal fins

Eq. (7) formalizes the symmetric/antisymmetric decomposition that follows naturally from the symmetry of the robot: by commanding the left and right actuators through mean and differential variables, as described in Table 3, the dominant effect of each variable on a single degree of freedom becomes explicit, as confirmed experimentally in Section 3.4.

$$\begin{aligned} A_1 &= A_m - \tfrac{1}{2}A_d, & \alpha_{u1} &= +\alpha_m - \tfrac{1}{2}\alpha_d, \\ A_2 &= -(A_m + \tfrac{1}{2}A_d), & \alpha_{u2} &= -(\alpha_m + \tfrac{1}{2}\alpha_d), \\ \alpha_1 &= A_1\sin(\omega t) + \alpha_{u1}, & \theta_1 &= \theta_m + \tfrac{1}{2}\theta_d, \\ \alpha_2 &= A_2\sin(\omega t) + \alpha_{u2}, & \theta_2 &= -\left(\theta_m - \tfrac{1}{2}\theta_d\right) \end{aligned} \tag{7}$$

This formulation is the central outcome of the modeling section since it reduces a highly nonlinear fluid–structure problem into a compact actuation interface that is directly usable by the low-level controllers described in Section 4.

3.4. Experimental validation of variable effects

Given the substantial simplifications adopted in the control-oriented model and the unknown coefficients appearing in the equations in Appendix, an experimental characterization was required. An analysis aimed at evaluating the swimming performances in relation to different actuation amplitudes and frequencies was carried out in our previous work (Bianchi et al., 2023b,a,c), where it was found that there is a linear relation between frequency and swimming speed. A periodic pitching rotation is present during flapping locomotion, but as frequency increases, its amplitude reduces due to the inertia of the central body. The robot is also capable of turning with a null curvature radius when it moves the fins with opposite angles ($A_m = 0$, $A_d \neq 0$). Specifically, we investigated how the input variables A_m, A_d, α_m, α_d, θ_m, and θ_d influence the robot's dynamic response.

The relationship between the mean oscillation of the pectoral fins A_m and the robot's longitudinal velocity had been previously investigated in Bianchi et al. (2023b), and an experimental test was performed to verify how the updated robot body changed this relationship, as shown in Fig. 7.

To analyze the remaining control variables, the main amplitude was fixed at $A_m = \pi/4$. After reaching the steady-state, different values of the control parameters were applied.

In Fig. 8, a clear relationship between A_d and the yaw rate ω_z is observed. Moreover, A_d introduces high-frequency oscillations in other degrees of freedom, attributed to the inertial effects of fins accelerating at different rates.

In Fig. 9, it can be seen that α_m has a weak influence on the angular velocities.

As shown in Fig. 10, a correlation emerges between α_d and the roll angle ϕ. No significant relationship is found between α_d and the yaw rate, and only minor effects appear on the other rotational velocities.

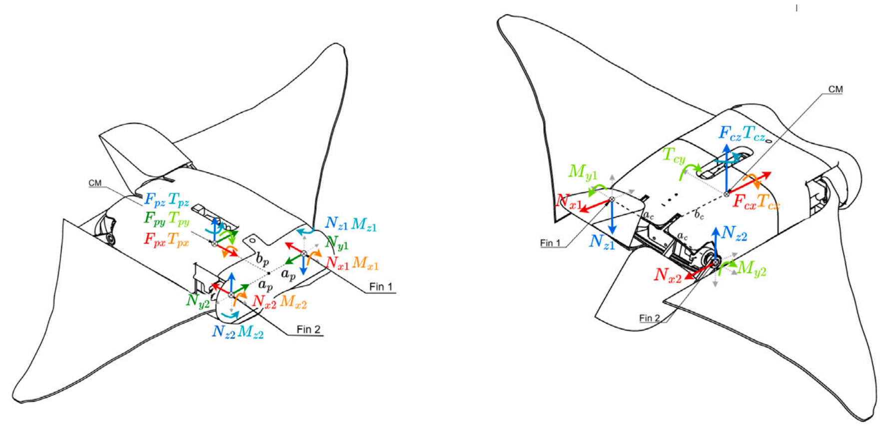

(a) Equivalent forces and moments applied to the center of mass, generated by the pectoral fin movement (b) Equivalent forces and moments applied to the center of mass, generated by the pectoral fin movement

Fig. 6. Equivalent forces and moments applied to the center of mass.

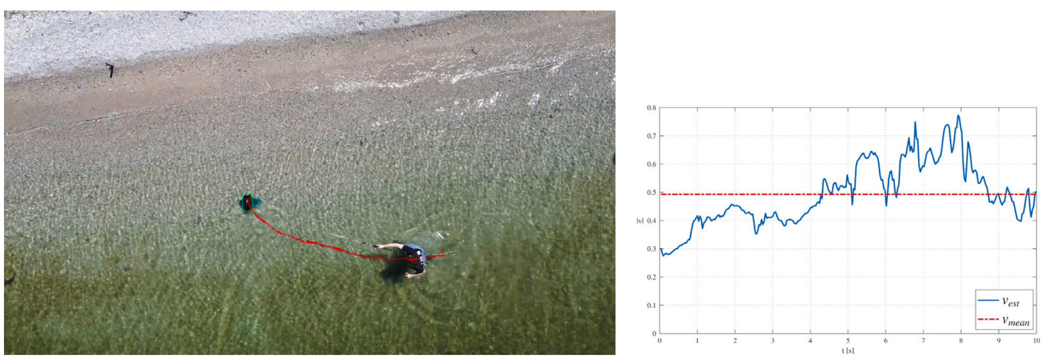

(a) Trajectory of the robot (b) Velocity for $A_m = \pi/4$

Fig. 7. Forward velocity of the robot without attitude control.

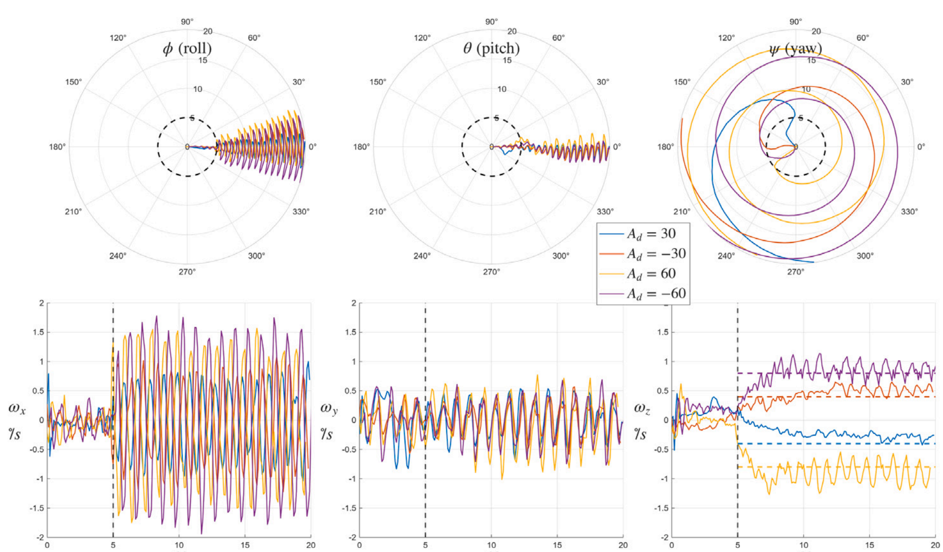

Fig. 8. Effects of A_d on the robot's orientation and angular velocity.

Fig. 11 shows the effects of θ_m, highlighting that variations in θ_m show a clear influence on the angular velocity ω_y. During the experiments, which were performed close to the water surface, positive values of θ_m were limited by surface contact, restricting the robot's pitch motion. In contrast, for negative θ_m, the robot was able to perform 360° front-flip rotations.

Finally, as shown in Fig. 12, θ_d has no significant effect on any degree of freedom.

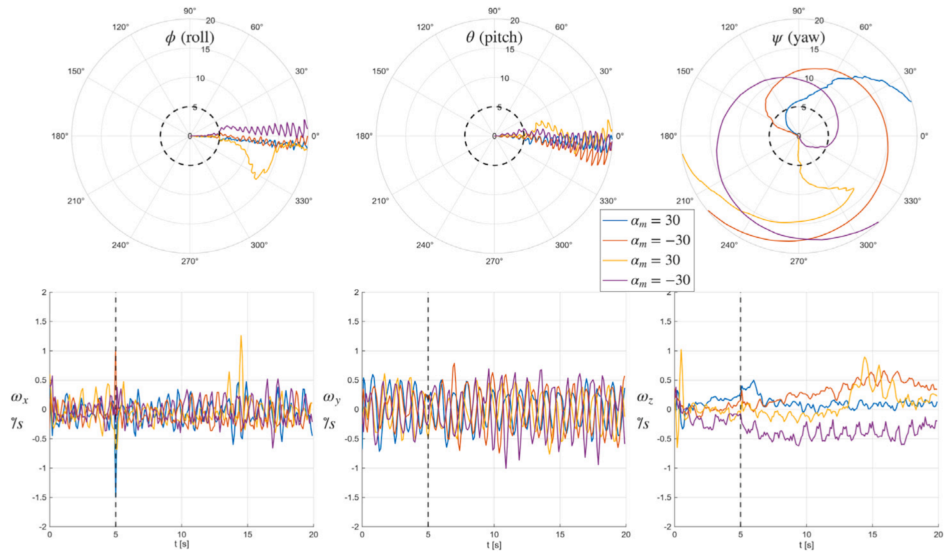

Fig. 9. Effects of α_m on the robot's orientation and angular velocity.

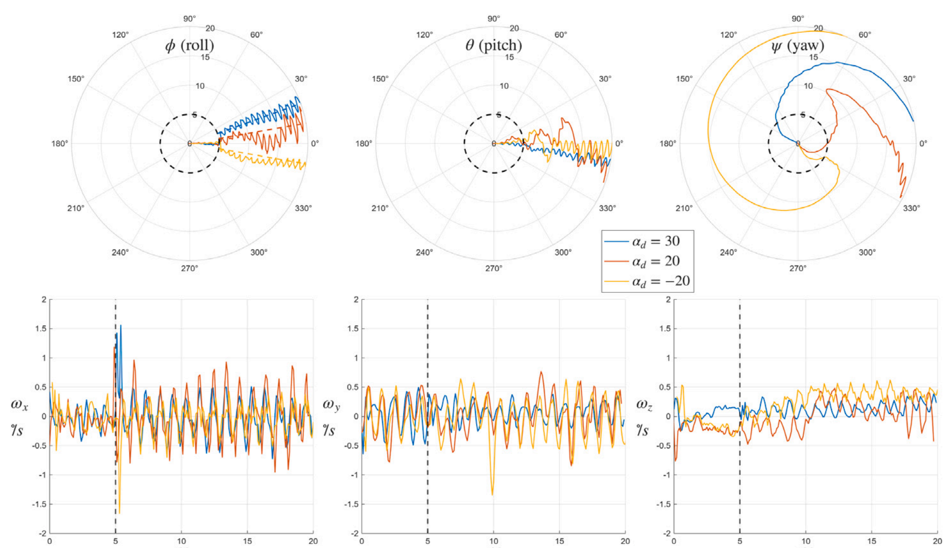

Fig. 10. Effects of α_d on the robot's orientation and angular velocity.

Table 4
Effects of kinematic variables on system response.

Input parameter	Dominant effect	Weaker effects
A_m	Forward thrust F_x	–
A_d	Yawing moment T_z	Rolling moment T_x; lateral force F_y
α_m	–	Pitching moment T_y; vertical force F_z
α_d	–	Rolling moment T_x
θ_m	Pitching moment T_y	Vertical force F_z; forward drag $-F_x$
θ_d	–	Rolling moment T_x; yawing moment T_z; forward drag $-F_x$

In conclusion, the experiments confirmed the relationships in Table 4.

The model therefore succeeds in providing a simple, reproducible, and experimentally consistent mapping from fin actuation to body motion for use in closed-loop control.

4. Control algorithm

To enable autonomous 6-DOF navigation using flexible pectoral fins, a cascaded control architecture was used following a hierarchical strategy commonly employed in state-of-the-art cruising AUVs (Hong et al., 2010-05; de Kruif et al., 2019; Garcia-Nava et al., 2023), composed of three hierarchical layers: a low-level attitude and angular-velocity controller acting on the kinematic fin variables introduced in Section 3; a high-level depth and planar navigation controller; and a feedforward thrust command regulating forward velocity.

The overall structure follows control practices used in conventional AUVs, adapted to the unique characteristics of a vehicle propelled by fins (Kokegei et al., 2008; Fenco et al., 2021). Controller setpoints are

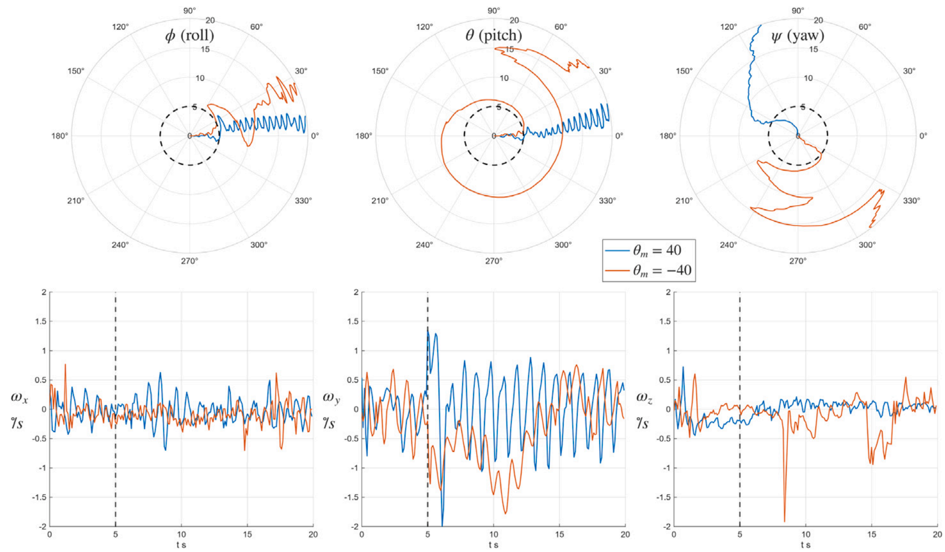

Fig. 11. Effects of θ_m on the robot's orientation and angular velocity.

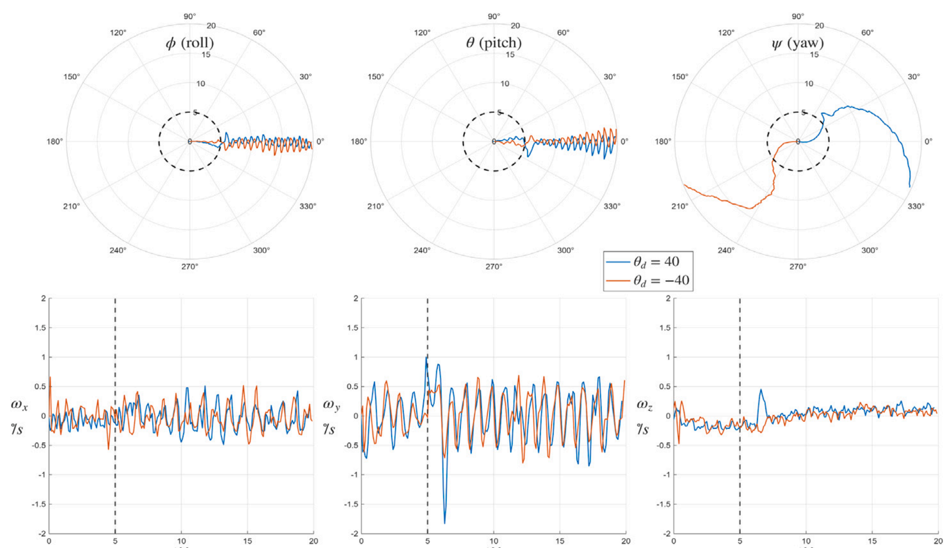

Fig. 12. Effects of θ_d on the robot's orientation and angular velocity.

scheduled within the platform actuation envelope, whose experimentally identified limits were analyzed in previous work (Bianchi et al., 2023b,a,c).

A key point of the proposed approach is that the fin actuation is parameterized by a reduced set of symmetric/antisymmetric kinematic variables, as shown in Section 3. While instantaneous fin motion generates coupled hydrodynamic and inertial effects, the experimental characterization in Table 4 shows that each variable has a dominant effect on one principal DOF over one fin period, while the remaining terms can be treated as bounded oscillatory disturbances that have no effect on average. This enables a control allocation in which each rotational axis is primarily driven by a single kinematic variable, summarized in Table 5.

4.1. State estimation

Accurate state estimation is essential for the controller to operate consistently in the presence of environmental disturbances. The robot's state consists of the orientation, represented by a quaternion, angular velocities, depth, and surface geodetic position, represented in latitude and longitude coordinates.

Table 5
Control allocation between feedback loops and kinematic fin variables.

Controlled quantity	Actuation variable	Force produced
Forward speed (feedforward)	A_m	F_x
Yaw rate/yaw	A_d	T_z
Pitch rate/pitch	θ_m	T_y
Roll rate/roll	α_d	T_x
Depth z	θ_{sp} $(Pitch_{SetPoint})$	Outer Loop

Orientation estimation. Orientation is estimated using the Madgwick filter, which fuses the measurements from the 3-axis gyroscope, accelerometer, and magnetometer. This filter provides quaternion estimates at a high rate with a bounded drift error, making it suitable for real-time onboard implementation (Madgwick et al., 2011). The Madgwick filter is updated at 100 Hz with parameter $\beta = 0.6$. Before each test, the sensor was kept stationary for a short initialization interval to allow bias convergence. Hard-iron and soft-iron calibration of the magnetometer was also performed. It corrects the drift introduced by gyroscope integration by exploiting absolute references available in the IMU measurements: the accelerometer provides the gravity direction,

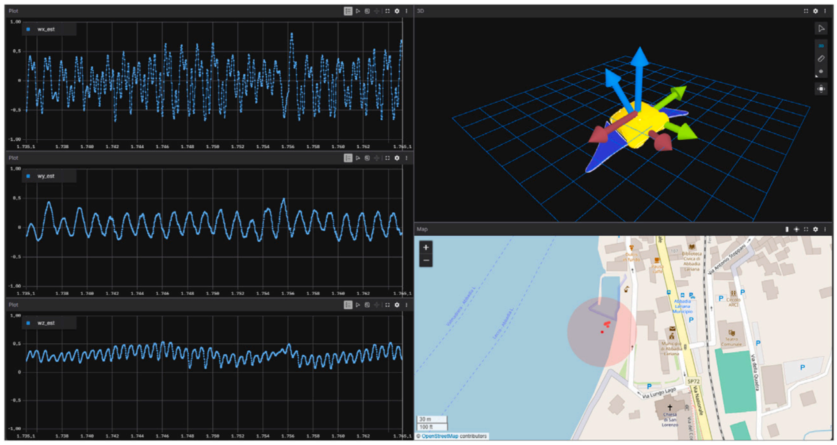

Fig. 13. Foxglove visualization of the robot's estimated state.

which is used to stabilize roll and pitch, while the magnetometer provides an absolute reference for yaw. As a result, long-term heading drift is bounded by the filter update rather than accumulating unboundedly over time. In the considered operating scenario, magnetic disturbances underwater were limited, making magnetometer-corrected yaw estimates sufficiently reliable for closed-loop heading control. For these experiments, no external ground-truth attitude measurement system was available; therefore, the attitude reported in 13 is intended to illustrate the estimated orientation used for control, rather than to provide a quantitative validation of absolute attitude accuracy.

For the estimation of the angular velocities, the raw IMU measurements are low-pass filtered to remove high-frequency components that could compromise the controller's robustness. This filtering is required because the attitude controller closes its fastest feedback loop on angular velocity. The output of this loop directly commands kinematic variables that map to joint angle motions, which in turn generate inertial forces associated with the moving components, as detailed in Appendix. This effect is particularly pronounced for caudal fin actuation, which is strongly coupled to the pitch dynamics. As a result, the variations in this degree of freedom at the oscillation frequency can propagate through the control loop. To mitigate this effect, the raw gyroscope measurements are low-pass filtered using a cutoff frequency of $\omega_{cut} = 1$ rad s^{-1}, thereby attenuating actuation-induced inertial disturbances.

Depth estimation. Depth is obtained from the absolute pressure sensor using the hydrostatic, reported in Eq. (8), with temperature compensation handled through libraries provided by the manufacturer.

$$z = \frac{p - p_0}{\rho g} \tag{8}$$

In-plane position estimation. During resurfacing events, GPS measurements are used to update the robot's position in the X-Y plane. When the robot is underwater, it operates in open-loop regarding planar position, while depth and attitude are always actively controlled. Although intermittent, the GPS data serve as coarse updates for target navigation, as shown in Section 5.

The estimated state of the robot is then visualized using Foxglove, as shown in Fig. 13, which illustrates the estimated attitude signals used by the control system during operation.

4.2. Orientation control

The orientation control is achieved through two nested feedback loops in velocity and position, as presented in Gołąbek et al. (2022). The innermost loop is responsible for angular velocity control and is composed of three decoupled PID controllers for each axis, reading a velocity setpoint ω_{i-sp} and the robot's estimated angular velocities $\hat{\omega}_i$, providing as output the kinematic variables associated with each degree of freedom $(A_d, \alpha_d, \theta_m)$.

The outermost loop is composed of a single quaternion-based proportional controller. This loop reads a quaternion setpoint q_{sp} provided by the high-level controller and uses as feedback the estimated orientation of the robot $\hat{q}$, returning the angular velocities ω_{sp}, in the robot's reference frame, necessary to correct the orientation error, as expressed in Eq. (9).

$$\begin{aligned} q_{\text{err}} &= q_{sp} \otimes \bar{\hat{q}} \\ q_u &= [\,1,\ 0,\ 0,\ 0\,] \\ q_\omega &= \overline{q_u} \otimes q_{\text{err}} \\ \boldsymbol{\omega}_{sp} &= -2k_p \left(\bar{\hat{q}} \otimes q_\omega \otimes \hat{q} \right)_v = -2k_p \left(\bar{\hat{q}} \otimes q_{sp} \right)_v \end{aligned} \tag{9}$$

This formulation enables fast, decoupled control of yaw, pitch, and roll while avoiding the nonlinearities and discontinuities associated with Euler-angle representations. It also mitigates cross-axis coupling effects introduced by the fin dynamics and reduces the impact of external disturbances, such as unknown water currents.

Controller tuning. The PID gains were tuned experimentally in water following the cascaded structure. First, the inner angular-velocity PID loops were tuned axis-by-axis by applying step changes to angular-rate setpoints and increasing gains until a fast response was achieved without sustained oscillations or actuator saturation. Next, the outer quaternion proportional gain k_p was increased until the desired attitude transient showed a sufficiently prompt response when tracking piecewise-constant orientation references, without saturating the actuation variables. Finally, the depth PID loop was tuned with the attitude controller enabled by applying depth steps and sinusoidal references and adjusting gains to minimize overshoot while maintaining stable tracking in the presence of current disturbances.

4.3. Position control

The outer control layer governs vertical and in-plane motion.

A PID controller tracks a commanded depth z_{sp} by modulating the pitch reference, considering that the vertical velocity depends on the pitching angle θ, as shown in Eq. (10). The output of this controller is the desired pitching angle θ_{sp}, which is used to compute the reference quaternion for the orientation control loop.

$$\dot{z} = \dot{x} \tan\theta \tag{10}$$

Regarding the $X - Y$ plane control, the robot receives a target position in geodetic coordinates $(\phi_{sp},\ \lambda_{sp})$ and, every time it receives a new position estimation from the GPS $(\hat{\phi},\ \hat{\lambda})$, it updates the in-plane

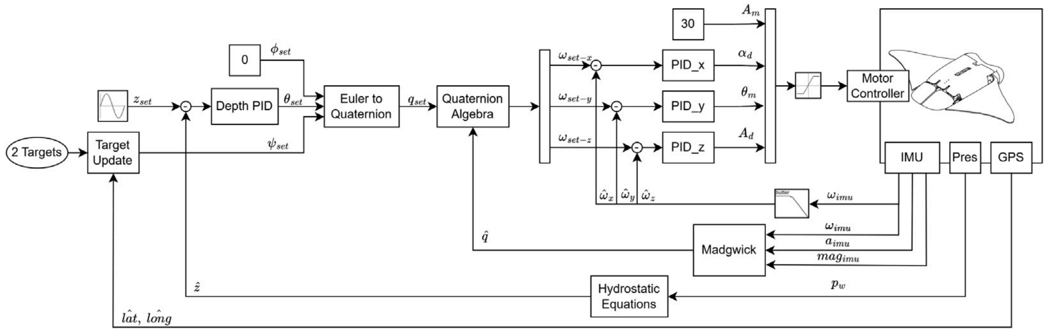

Fig. 14. Overall control architecture.

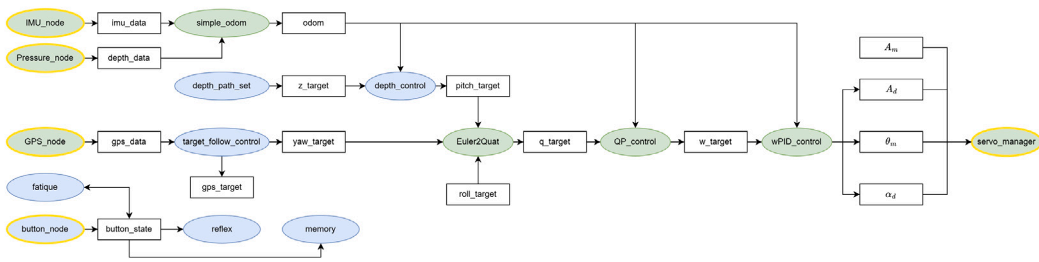

Fig. 15. Software block diagram: circles represent nodes and squares represent topics; nodes in green are written in C++, while nodes in blue are written in Python; a yellow contour indicates that the node communicates with hardware.

heading direction ψ_{sp} to guide the robot to the target. Between GPS updates, the robot preserves its last reference yaw.

The remaining roll angle setpoint ϕ_{sp} for the creation of the heading quaternion setpoint is set to zero to maintain overall robot stability.

This separation between attitude control and planar guidance ensures robust behavior despite intermittent surface-position measurements.

Finally, the overall controller architecture can be seen in Fig. 14.

4.4. Implementation

The control architecture is implemented within ROS2 Jazzy. Real-time control and estimation nodes run in C++ for performance, while high-level mission handling is implemented in Python as described in Fig. 15. A physical button triggers mission start, and the system includes automatic timeout termination for safety. The modular ROS architecture enables straightforward integration of additional sensors and navigation algorithms.

All the software that was present on the robot is publicly available at the following repository (Scudeletti, 2025).

5. Experimental results

After implementing the control architecture and state estimation algorithms, the next step involved an experimental phase aimed at validating the overall system performance in open water.

Basing on the swimming performance characterization of the robot performed in previous work, e.g., forward-speed dependence on fin flapping parameters and maneuverability under open-loop gait modulation (Bianchi et al., 2023b,a,c), these experimental tests are aimed at assessing the closed-loop control for navigation using onboard sensing in open-water conditions.

In this environment, natural water currents act as external disturbances that the robot must compensate for in order to maintain the desired orientation and reach the reference position. A total of four experiments were conducted to evaluate the effectiveness and robustness of the implemented control architecture. The first two focused on assessing the performance of the inner orientation control loop, while the remaining tests examined the behavior of the outer position-tracking layers. In all cases, the mean fin oscillation amplitude A_m was kept constant at $\pi/6$ to maintain a constant forward velocity reference of 0.3 m/s throughout the experiments.

The outcome of these tests is the robot's position and orientation, and, while the orientation and the depth are measured directly by the robot, its position in the plane is computed in post-processing by analyzing the video recorded by a drone. The adopted drone is a DJI Mini 4 Pro capturing 4K videos in a top-down view; its height is kept constant throughout the whole duration of the test, and its position obtained from its internal GPS is measured and stored in the video metadata. Then, the robot's position is analyzed using the MATLAB Image Processing Toolbox, reconstructing its position in the image, and, given the drone's height and position, its position in latitude and longitude is reconstructed and considered as ground-truth.

To strengthen the evaluation, each experiment was quantified using standard performance metrics that capture tracking accuracy and oscillatory behavior. Specifically, we evaluate the tracking error $e(t)$, the root-mean-square error (RMSE), the steady-state bias, and the oscillatory error at the fin actuation frequency, as summarized in Table 6. These metrics were computed from the recorded test data using the estimated attitude $\hat{q}$, the setpoint quaternion q_{set} derived from ψ_{set} and θ_{set}, and the estimated depth $\hat{z}$ (with setpoint z_{set} for depth-controlled tests).

5.1. Experiment 1: Attitude maintenance

The first test evaluated the robot's ability to maintain a prescribed orientation. For this purpose, the robot was initially positioned in the water and held stationary. Upon pressing the control button, the onboard controller was activated: the target orientation q_{target} and depth z_{target} were set equal to the estimated values q_{est} and z_{est} at the instant when the button is pressed, and kept constant throughout the test.

Figs. 16 show the estimated and reference orientations, where the quaternions are decomposed into the corresponding Euler angles for clarity, and Table 7 shows the metrics from the resulting error.

Table 6
Performance metrics used to quantify tracking accuracy.

Metric	Definition
Tracking error	$e(t) = x_{set}(t) - x(t)$.
Root Mean Square Error (RMSE)	$\sqrt{\frac{1}{T}\int_0^T e(t)^2\,dt}$.
Steady-state bias	$b_{ss} = \frac{1}{\Delta T}\int_{T-\Delta T}^{T} e(t)\,dt$, with $\Delta T = 5\,\text{s}$.
Oscillatory error at fin actuation frequency	Magnitude of the harmonic component of $e(t)$ at $f_0 = 0.8\,\text{Hz}$ (fin oscillation frequency, kept constant across tests).

Table 7
Test 1 – performance metrics.

Axis	RMSE	Steady-state bias	Oscillation at 0.8 Hz
Roll	3.5°	0.008°	0.6°
Pitch	4.4°	0.1°	0.3°
Yaw	1.3°	0.006°	0.35°

Table 8
Test 2 – performance metrics.

Axis	RMSE	Steady-state bias	Oscillation at 0.8 Hz
Roll	9.16°	−1.2°	6.7°
Pitch	12.8°	2.8°	6.5°
Yaw	65.6°	45.3°	1.8°

Analysis. Test 1 validates the baseline stability of the inner attitude loop under real open-water disturbances. The low RMSE and near-zero steady-state bias across all axes indicate that the proposed fin-parameter actuation interface is sufficient for setpoint regulation, while the small 0.8 Hz component confirms that actuation-induced oscillations remain bounded and do not destabilize the closed loop.

Finally, Fig. 17 illustrates the full trajectory reconstructed from drone video of the experiment, providing a visual overview of the robot's behavior during the orientation maintenance test.

5.2. Experiment 2: Tracking a rotating attitude reference

The second orientation-control experiment evaluated the robot's ability to track a rotating reference.

As in the previous test, the experiment began with the robot stationary in the water. Upon pressing the control button, the reference depth z_{ref} was initialized to the last estimated value z_{est}, while the orientation reference ψ_{set} evolved dynamically according to Eq. (11),

$$\psi_{set} = \psi_0 + \omega t \tag{11}$$

where ψ_0 corresponds to the most recent estimated orientation ψ_{mes} at the moment of activation, and ω is the predefined angular rate selected prior to the experiment.

The results for one of the tests conducted with $\omega = 0.5$ rad s^{-1} are presented in Fig. 18, following the same format as the previous orientation-maintenance experiment, and Table 8 shows the metrics obtained. The corresponding trajectory reconstructed from drone video is shown in Fig. 19, illustrating the robot's response to a continuously varying reference.

Analysis. In Test 2, the tracking performance differs across axes because yaw is primarily limited by actuation saturation when following a continuously rotating reference. Roll and pitch remain bounded around the commanded motion, whereas yaw exhibits a repeatable phase lag, which is consistent with a finite achievable yaw acceleration.

Table 9
Test parameters.

Parameter	Value
ω_{yaw}	0.3 rad s^{-1}
A_z	0.2 m
T_z	20 s
z_{offset}	0.3 m

Table 10
Test 3 – performance metrics.

Axis	RMSE	Steady-state bias	Oscillation at 0.8 Hz
Roll	11.2°	−1.47°	2.4°
Pitch	17.4°	25.7°	3.0°
Yaw	21.9°	29.9°	1.1°
Depth	0.073 m	0.068 m	0.017 m

5.3. Experiment 3: Helical trajectory with depth modulation

Moving to the outer layer of the control architecture, the third experiment was designed to evaluate the robot's ability to regulate its depth. In this test, a helical trajectory was generated by combining the rotating orientation reference with a sinusoidal depth command defined by Eq. (12):

$$z_{ref} = A_z \sin\left(\frac{t}{T_z}\right) - z_{off} \tag{12}$$

Here, the parameters A_z, T_z, and z_{off} were predetermined to produce a fully submerged sinusoidal motion, ensuring that $A_z < z_{off}$ so that the trajectory remained entirely below the water surface.

Results from one of these experiments, with setpoint values in Table 9, are shown in Fig. 20, and the performances are studied in Table 10. The complete 3D trajectory reconstructed from drone video is presented in Fig. 21, clearly illustrating the helical path executed by the robot.

Analysis. Test 3 couples the depth outer loop with the attitude controller while the yaw reference rotates, producing a 3D helical motion. The depth RMSE and limited oscillatory error show that modulating pitch for vertical control (Eq. (10)) remains effective even in the presence of fin-induced periodic disturbances and current-induced bias.

5.4. Experiment 4: Multi-target navigation

Finally, to evaluate the full control architecture of the robot, a fourth test was conducted involving simultaneous commands to both high-level controllers.

In this experiment, the depth controller was assigned a sinusoidal reference similar to the previous test, but with parameters chosen such that $A_z > z_{off}$. This configuration allowed the robot to periodically resurface at each cycle, enabling GPS data acquisition for improved position estimation.

Meanwhile, the target controller was provided with two distinct position setpoints. The robot was instructed to switch from one target to the other once it reached a predefined proximity threshold relative

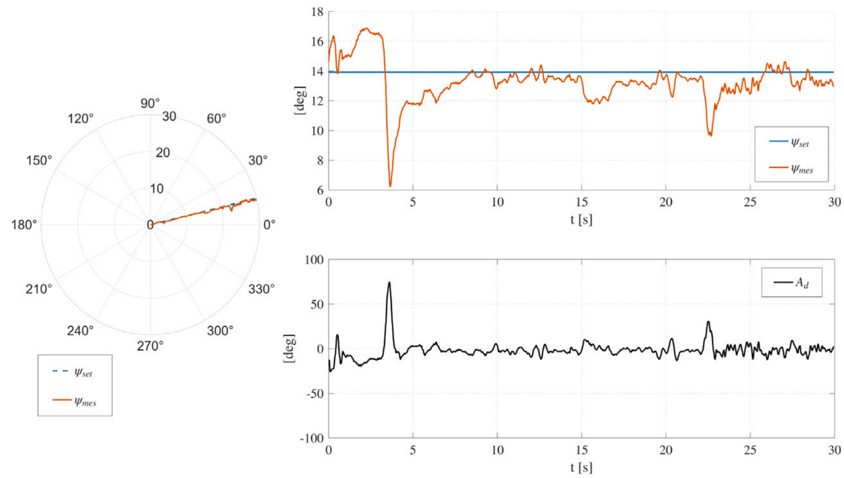

(a) Yaw control

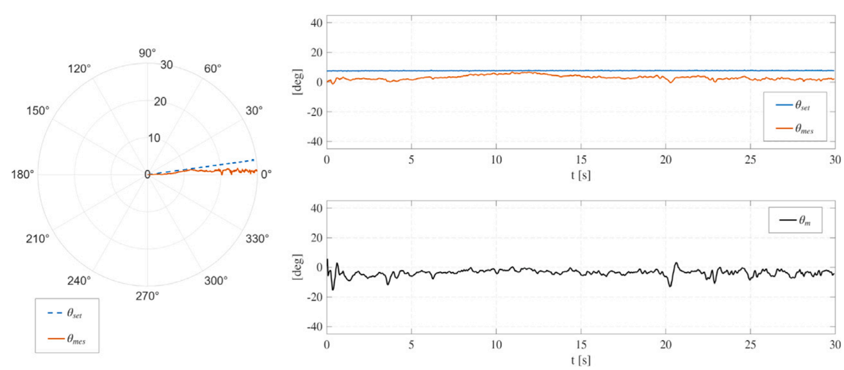

(b) Pitch control

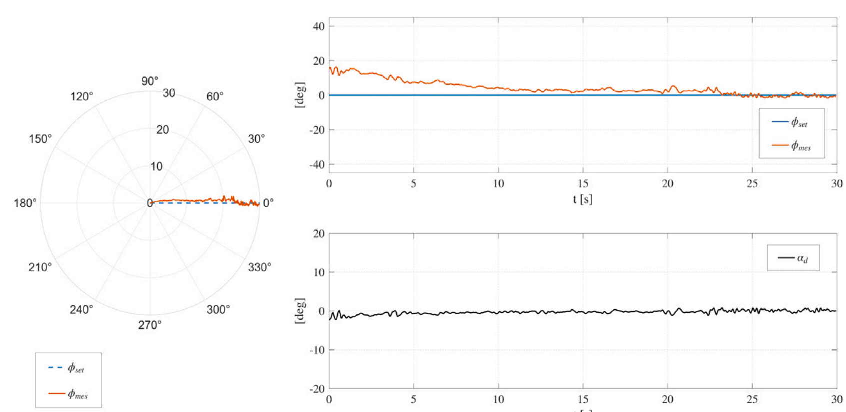

(c) Roll control

Fig. 16. Test 1 — Attitude control. Each sub-figure includes: on the left, a polar plot comparing the reference angle (blue) and the measured angle (red); on the right: two time-domain plots showing (top) the tracking error between the reference (blue) and measured angle (red), and (bottom) the associated control input (black).

to the current goal. This test was conducted over an extended period to assess the long-term performance of the controller under realistic operating conditions.

The results illustrate the overall performance of the proposed control system. Fig. 22(a) shows the behavior of the depth controller, highlighting its ability to track the resurfacing trajectory accurately, while Fig. 22(b) shows the ability of the orientation controller to follow the discrete orientation setpoints on the yaw axis coming from the target controller. Their performance is evaluated in Tables 11 and 12, where the experiment is partitioned into a dynamic phase, in which the controller continuously updates the setpoint, and a stable phase, during which setpoint updates are minimized. Finally, the complete path followed by the robot during the experiment is reported in Fig. 23 with respect to the given targets.

Fig. 17. Test 1 — Track from drone recording.

Table 11
Test 4 – performance metrics in the first 90 s (dynamic phase).

Axis	RMSE	Steady-state bias	Oscillation at 0.8 Hz
Roll	11.6°	8.15°	3.0°
Pitch	15.0°	−4.7°	3.8°
Yaw	87.4°	N.D.	7.0°
Depth	0.04 m	0.023 m	0.011 m

Table 12
Test 4 – performance metrics in the last 90 s (static phase).

Axis	RMSE	Steady-state bias	Oscillation at 0.8 Hz
Roll	12.4°	7.5°	5.7°
Pitch	13.0°	15.7°	9.0°
Yaw	32.3°	N.D.	1.5°
Depth	0.027 m	0.015 m	0.015 m

Analysis. Test 4 evaluates the complete control algorithm. The dynamic RMSE (Table 11) mainly reflects aggressive yaw setpoint changes caused by noisy GPS fixes near the waterline, rather than instability of the attitude loop. The static RMSE (Table 12) shows improved tracking once the heading setpoint becomes less variable, highlighting that the present limitation for waypoint convergence is primarily sensing accuracy rather than controllability of the fin-actuated platform.

6. Discussion

The experimental results indicate both the performance of the proposed controller and the validity of the control-oriented abstraction, which treats fins as generalized thrusters. This abstraction is shown to be sufficient to achieve repeatable closed-loop stabilization and basic navigation tasks in open water, even in the presence of wave-induced disturbances and periodic actuation effects.

6.1. Attitude control performance

Across trials, the attitude loop remained stable and provided consistent regulation, with the main limitations arising from actuator saturation during aggressive maneuvers or when more degrees of freedom need to be corrected simultaneously. This last effect is partially solved by assigning a priority to different DOFs, making yaw and pitch control more important than roll control. However, yaw rotational speed is limited by the finite moment that can be generated through differential fin actuation; when the desired rate exceeds this capability, the controller still produces a response but converges with a constant phase lag rather than eliminating the error instantaneously. This behavior is consistent with the tuning choices discussed in the control section and provides a practical guideline for reference design: heading setpoints should be scheduled considering the achievable yaw acceleration.

A second recurring feature is the presence of oscillatory components in roll, pitch, and depth at the fin-flapping frequency. These oscillations are expected for fin-driven platforms because the actuation introduces periodic inertial contributions that cannot be fully removed by low-pass filtering without degrading responsiveness. In the presented experiments, the oscillations remain bounded and do not compromise stability; therefore, the proposed strategy effectively regulates the mean attitude while tolerating periodic components intrinsic to the propulsion mechanism.

6.2. Depth control behavior

Depth regulation remained reliable across both smooth and intermittent profiles. The small residual tendency to surface is consistent with the vehicle's positive buoyancy and the restoring moments from the offset between the centers of mass and buoyancy. Despite this bias, the controller maintained stable depth tracking and effectively compensated for the disturbance, indicating robust control performance. While not critical for the demonstrated navigation tasks, this behavior shows the importance of precise buoyancy trimming when tighter depth tolerances are required.

6.3. Planar navigation and GPS limitations

The multitarget experiment highlights that the overall navigation performance is currently limited by sensing rather than control. While the heading loop provides repeatable tracking, the single-frequency GPS used during resurfacing is vulnerable to multipath and attenuation near the waterline, which can lead to inconsistent target switching and missed convergence (Fig. 24).

The experimental campaign not only evaluates controller performance, but also provides direct validation of the main contribution of this work, namely the definition of a control-oriented framework that enables fin-actuated systems to be treated analogously to thruster-driven AUVs. The attitude control experiments demonstrate that the proposed parametrization of fin kinematics allows stable and approximately decoupled regulation of roll, pitch, and yaw. This result is non-trivial for flexible-finned systems, where actuation typically produces strongly coupled and nonlinear effects, and confirms that the reduced set of control variables introduced in Section 3 provides a

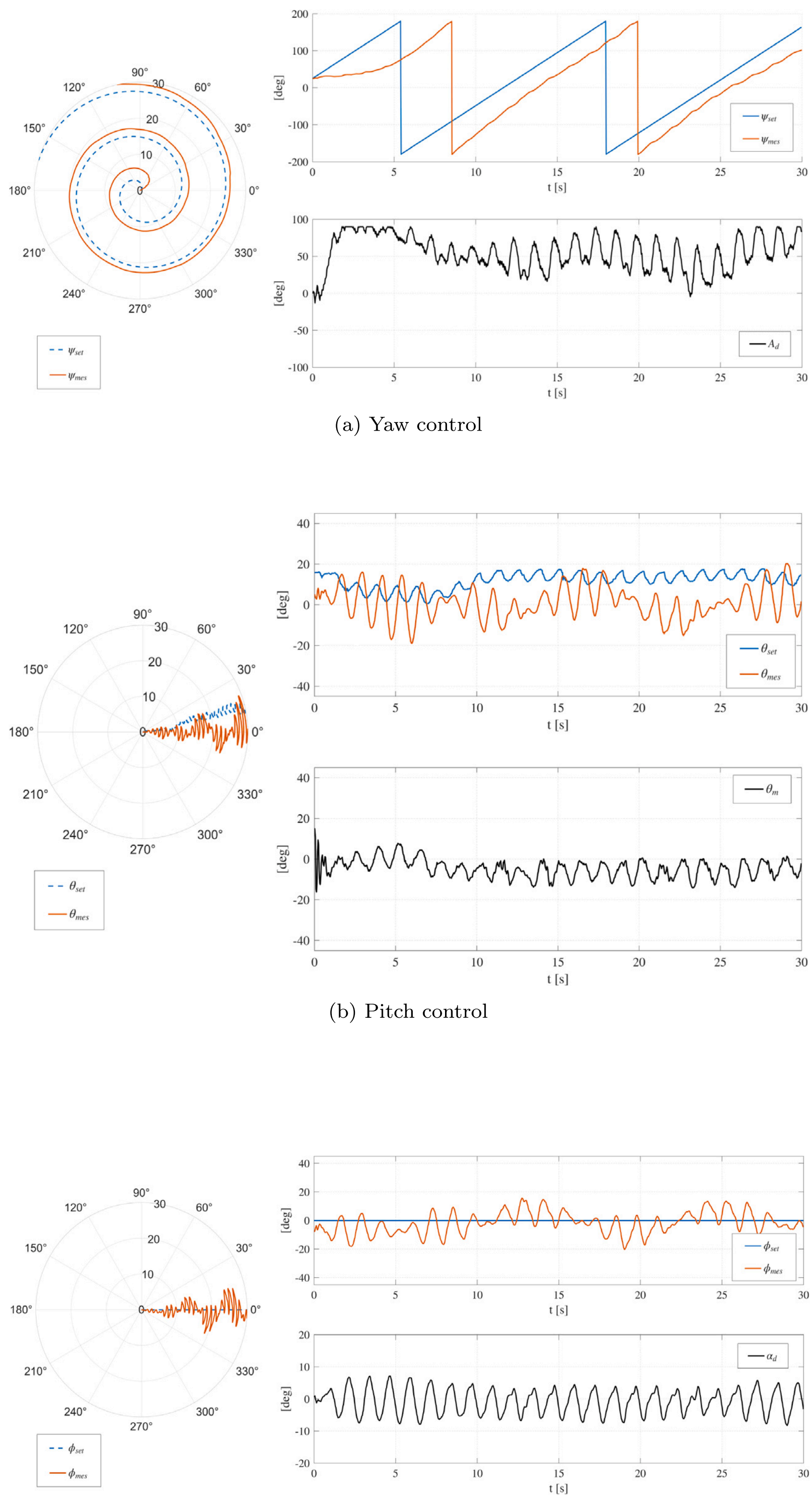

(a) Yaw control

(b) Pitch control

(c) Roll control

Fig. 18. Test 2 — Attitude control.

practical interface for implementing classical cascaded control strategies. The depth and helical trajectory experiments further validate this abstraction by showing that independent control loops can be combined to achieve coordinated three-dimensional motion. This demonstrates that the proposed framework supports full 6-DOF regulation without relying on a detailed hydrodynamic model, which is a key requirement

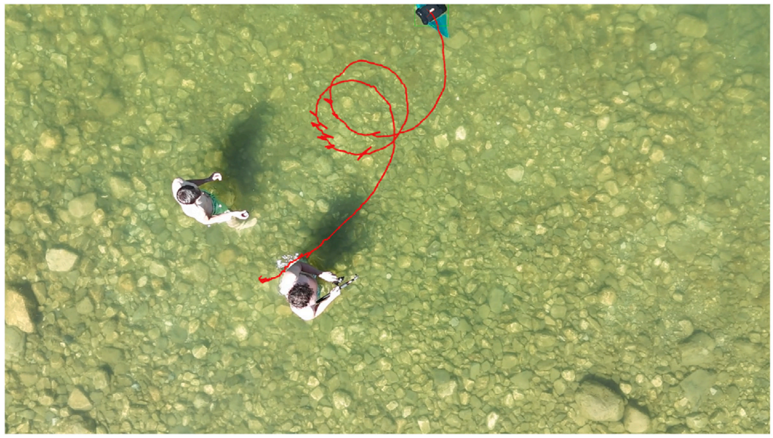

Fig. 19. Test 2 — Track from drone recording.

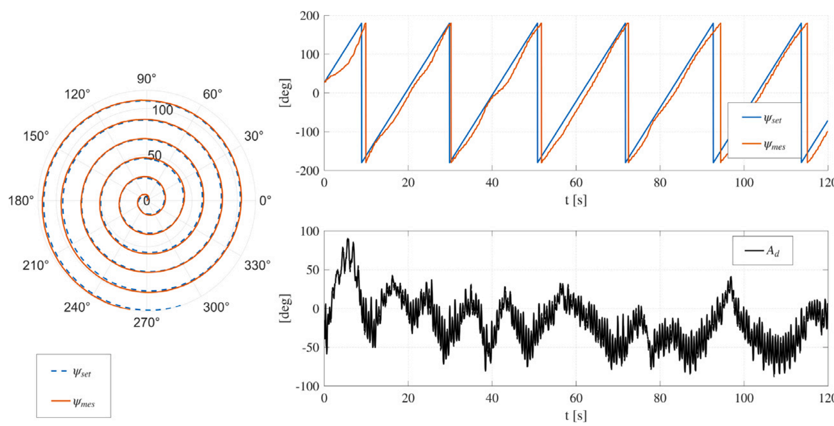

(a) Yaw control

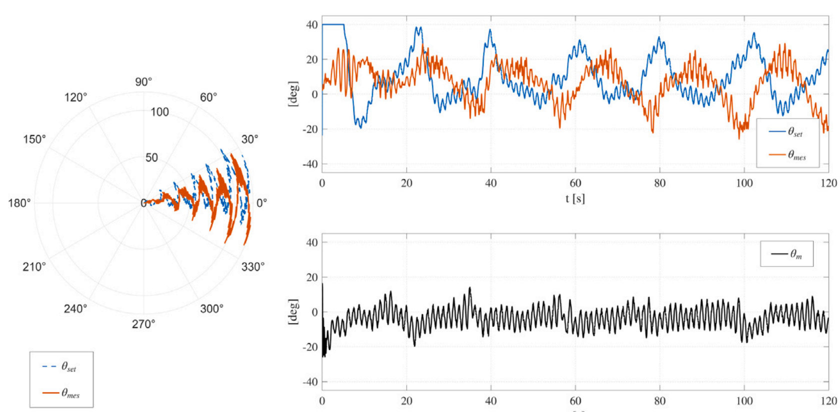

(b) Pitch control

Fig. 20. Test 3 — Attitude and depth control.

for practical onboard implementation. Finally, the multi-target navigation experiment highlights the effectiveness of the complete onboard architecture. Although global navigation accuracy is affected by GPS limitations, the stability and responsiveness of the inner control loops remain consistent. This confirms that the proposed control strategy is robust, and that the main limitation of the current system lies in sensing and localization rather than in control design. Overall, these results show that the novelty of the proposed approach lies in the integration of a simplified, model-independent control representation with a fully onboard navigation architecture, enabling autonomous operation of a batoid-inspired AUV in real open-water conditions.

7. Conclusions

Through a simplified analysis of the robot's dynamics, it was possible to establish a reduced set of kinematic variables that map

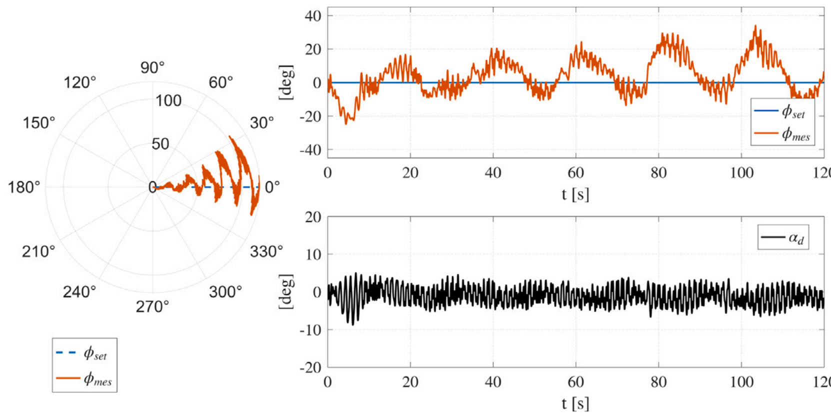

(c) Roll control

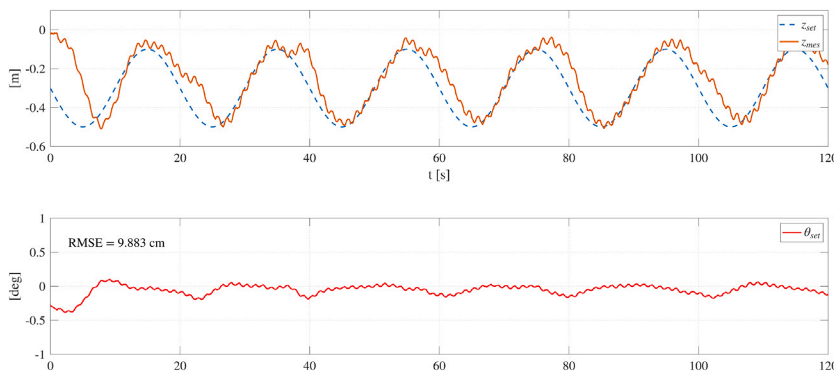

(d) Depth control

Fig. 20. (*continued*).

Fig. 21. Test 3 — Track from drone recording.

actuator inputs to the resulting body motions. This abstraction allowed the identification of control variables suitable for regulating the robot's motion underwater while maintaining a decoupled representation of the controllable degrees of freedom.

This study guided the design of an experimentally tuned low-level controller focused on attitude stabilization and longitudinal velocity regulation. To allow this abstraction, a model-independent estimation and control strategy was introduced to guide the robot in three-dimensional space, relying solely on the experimentally tuned low-level loops and the derived kinematic variables.

The resulting architecture was validated in open-water experiments using higher-level controllers for depth regulation and GPS-based target following. Key performance trends are summarized in Tables 11 and 12 and qualitatively illustrated in Fig. 22.

The inner-loop attitude stabilization achieved root mean square errors (RMSEs) of 1.3° for yaw, 4.4° for pitch, and 3.5° for roll during the open-water orientation-maintenance test, as shown in Table 7. Evaluation in a rotating reference frame produced comparable performance; however, actuation delay emerged as the primary limitation, reducing effective control bandwidth and resulting in slightly degraded transient

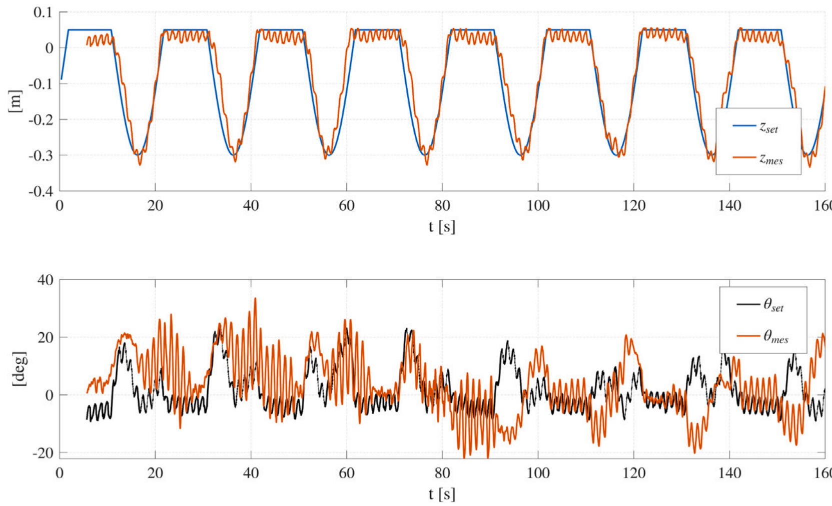

(a) Depth control

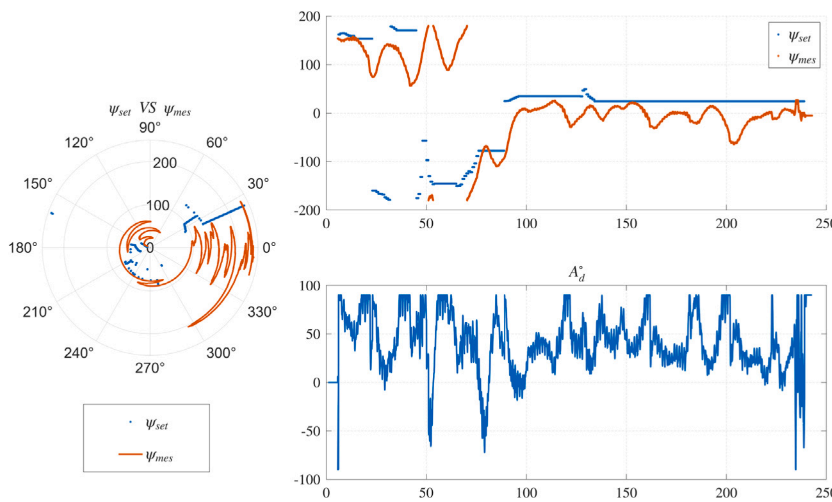

(b) Yaw control

Fig. 22. Test 4 — Target following control.

Fig. 23. Test 4 — path followed.

response and tracking accuracy at higher rotation rates. When attitude and depth control were coupled to generate three-dimensional helical motion, the depth outer loop achieved a tracking RMSE of 0.073 m with limited periodic oscillations, as shown in Table 10. In multi-target navigation, after the heading setpoint variability decreased, the GPS-assisted guidance phase yielded a depth RMSE of 0.027 m and a yaw RMSE of 32.3°, as shown in Table 12. These results indicate that overall waypoint convergence is primarily constrained by sensing and localization quality rather than by poor stability of the control algorithm. These results quantitatively support the effectiveness of the proposed control-oriented framework for real-world deployment.

The system demonstrated reliable orientation stabilization, accurate tracking of dynamic attitude and depth references, execution of helical trajectories, and preliminary waypoint navigation under GPS-assisted guidance.

The experimental validation remains constrained by actuator saturation and by reliance on surface GNSS for global position updates, as no absolute position feedback is available while the robot is submerged, and localization drift between surfacing events due to the lack of a

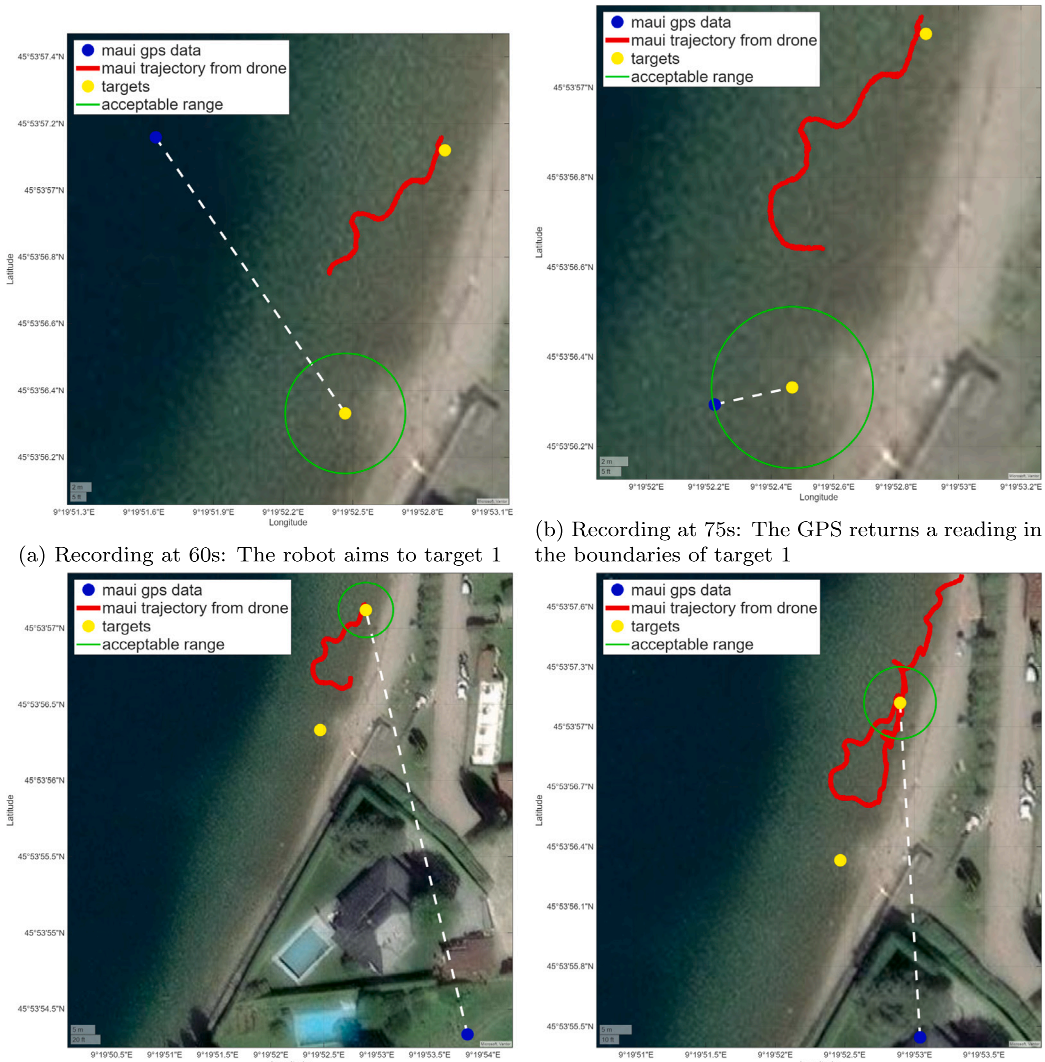

(a) Recording at 60s: The robot aims to target 1

(b) Recording at 75s: The GPS returns a reading in the boundaries of target 1

(c) Recording at 90s: The Robot is heading to target 2

(d) Recording at 200s: The GPS never returns readings inside the boundaries of target 2

Fig. 24. Test 4 — Analysis of the target following control from recordings.

lightweight, easily integrated underwater localization sensor suite on the current platform.

The main contribution of this work is the demonstration of a simple and accessible methodology for designing and controlling a soft, bioinspired underwater robot capable of basic autonomous navigation, achieved through a model-independent parametrization of fin actuation and a control strategy derived from a simplified analysis of actuator dynamics. The results support the claim that this abstraction can deliver a practical 6-DOF regulation in real environments.

Building on these results, future developments will focus on improved surface positioning (eg., multi-band GNSS) and tighter sensor calibration, fusion of GPS with onboard vision or acoustic localization to reduce drift and extend submerged navigation, development of a more accurate model for precise control tuning and filtering of actuator-induced disturbances, and evaluation of adaptive and learning-based control strategies to handle uncertain hydrodynamics and environmental disturbances.

CRediT authorship contribution statement

Tommaso Scudeletti: Writing – review & editing, Writing – original draft, Visualization, Validation, Software, Methodology, Investigation, Formal analysis, Data curation. **Giovanni Bianchi:** Writing – review & editing, Writing – original draft, Validation, Supervision, Methodology, Investigation, Formal analysis, Conceptualization. **Stefano Arrigoni:** Visualization, Investigation. **Simone Cinquemani:** Supervision, Resources, Project administration, Funding acquisition, Conceptualization. **Francesco Braghin:** Supervision, Resources, Project administration, Funding acquisition.

Declaration of competing interest

The authors declare that they have no known competing financial interests or personal relationships that could have appeared to influence the work reported in this paper.

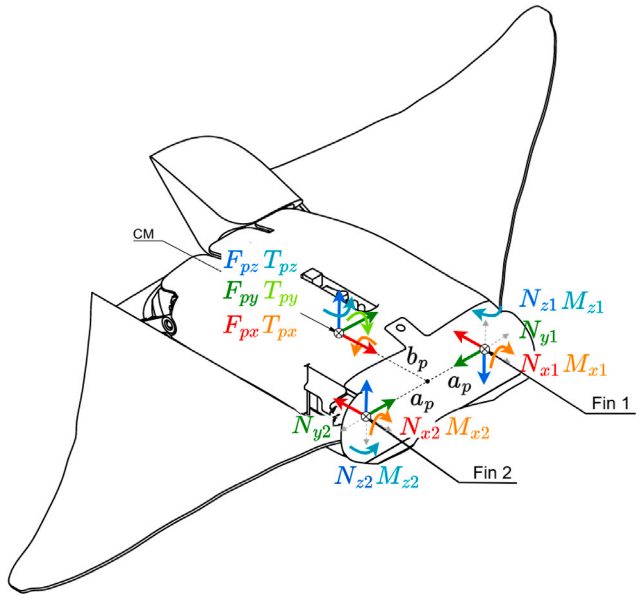

Fig. A.25. Equivalent forces and moments applied to the center of mass, generated by the pectoral fin movement.

Appendix. Mathematical study of the control-oriented fin-body dynamics

A.1. Constraint forces on fin i generated by pectoral fin movement

$$\begin{aligned}
&\qquad\qquad Hydrodynamic && \qquad Inertial \\
N_{xi} &= -f_x(A_i,\omega_i) && \\
N_{yi} &= -f_{yz}(A_i,\omega_i)\cos(\alpha_{ui}) && -F_{ci}\cos(\alpha_i) - F_{Ii}\sin(\alpha_i) \\
N_{zi} &= -f_{yz}(A_i,\omega_i)\sin(\alpha_{ui}) && -F_{ci}\sin(\alpha_i) + F_{Ii}\cos(\alpha_i) \\
M_{xi} &= && T_{Ii} + F_{Ii} l_p \\
M_{zi} &= f_{le}(A_i,\omega_i) d_{le} &&
\end{aligned} \tag{A.1}$$

A.2. Constraint forces of the 2 pectoral fins brought to the center of mass of the robot

See Fig. A.25.

$$\begin{aligned}
F_{px} &= -(N_{x1}+N_{x2}) \\
&= f_x(A_1,\omega_1) + f_x(A_2,\omega_2) \\
F_{py} &= -(N_{y1}-N_{y2}) \\
&= \left[f_{yz}(A_1,\omega_1)\cos\alpha_{u1} - f_{yz}(A_2,\omega_2)\cos\alpha_{u2}\right] \\
&\quad + \left[F_c(\dot\alpha_1)\cos\alpha_1 - F_c(\dot\alpha_2)\cos\alpha_2\right] \\
&\quad + \left[F_I(\ddot\alpha_1)\sin\alpha_1 - F_I(\ddot\alpha_2)\sin\alpha_2\right] \\
F_{pz} &= -(N_{z1}-N_{z2}) \\
&= \left[f_{yz}(A_1,\omega_1)\sin\alpha_{u1} - f_{yz}(A_2,\omega_2)\sin\alpha_{u2}\right] \\
&\quad + \left[F_c(\dot\alpha_1)\sin\alpha_1 - F_c(\dot\alpha_2)\sin\alpha_2\right] \\
&\quad - \left[F_I(\ddot\alpha_1)\cos\alpha_1 - F_I(\ddot\alpha_2)\cos\alpha_2\right]
\end{aligned} \tag{A.2}$$

$$\begin{aligned}
T_{px} &= -(M_{x1}+M_{x2}) - a_p(N_{z1}+N_{z2}) \\
&= a_p\left[f_{yz}(A_1,\omega_1)\sin\alpha_{u1} + f_{yz}(A_2,\omega_2)\sin\alpha_{u2}\right] \\
&\quad + a_p\left[F_c(\dot\alpha_1)\sin\alpha_1 + F_c(\dot\alpha_2)\sin\alpha_2\right] \\
&\quad - a_p\left[F_I(\ddot\alpha_1)\cos\alpha_1 + F_I(\ddot\alpha_2)\cos\alpha_2\right] \\
&\quad - \left[M_{x1}(\ddot\alpha_1) + M_{x2}(\ddot\alpha_2)\right] \\
T_{py} &= b_p(N_{z1}-N_{z2}) \\
&= -b_p\left[f_{yz}(A_1,\omega_1)\sin\alpha_{u1} - f_{yz}(A_2,\omega_2)\sin\alpha_{u2}\right] \\
&\quad - b_p\left[F_c(\dot\alpha_1)\sin\alpha_1 - F_c(\dot\alpha_2)\sin\alpha_2\right] \\
&\quad + b_p\left[F_I(\ddot\alpha_1)\cos\alpha_1 - F_I(\ddot\alpha_2)\cos\alpha_2\right] \\
T_{pz} &= M_{z1} - M_{z2} + a_p(N_{x1}-N_{x2}) - b_p(N_{z1}-N_{z2}) \\
&= d_{le}\left[f_{le}(A_1,\omega_1) - f_{le}(A_2,\omega_2)\right] \\
&\quad a_p\left[f_x(A_1,\omega_1) - f_x(A_2,\omega_2)\right] \\
&\quad + b_p\left[f_{yz}(A_1,\omega_1)\sin\alpha_{u1} - f_{yz}(A_2,\omega_2)\sin\alpha_{u2}\right] \\
&\quad + b_p\left[F_c(\dot\alpha_1)\sin\alpha_1 - F_c(\dot\alpha_2)\sin\alpha_2\right] \\
&\quad - b_p\left[F_I(\ddot\alpha_1)\cos\alpha_1 - F_I(\ddot\alpha_2)\cos\alpha_2\right]
\end{aligned} \tag{A.3}$$

A.3. Relationships between pectoral kinematic variables and forces on the axis

See Fig. A.26.

A.4. Constraint forces on fin i generated by caudal fin movement

$$\begin{aligned}
&\qquad Hydrodynamic && \qquad Inertial \\
N_{xi} &= K_d(\dot x)\sin(\theta_i)^2 && +F_{ci}(\dot\theta_i)\cos(\theta_i) + F_I(\ddot\theta_i)\sin(\theta_i) \\
N_{zi} &= K_d(\dot x)\sin(\theta_i)\cos(\theta_i) && -F_c(\dot\theta_i)\sin(\theta_i) + F_I(\ddot\theta_i)\cos(\theta_i) \\
M_{yi} &= K_d(\dot x)\sin(\theta_i) l_c && T_I(\ddot\theta_i) + F_I(\ddot\theta_i) l_c
\end{aligned} \tag{A.4}$$

A.5. Constraint forces of the 2 caudal fins brought to the center of mass of the robot

See Fig. A.27.

$$\begin{aligned}
F_{cx} &= -(N_{x1}+N_{x2}) \\
&= -K_d(\dot x)\left[\sin^2\theta_1 + \sin^2\theta_2\right] \\
&\quad - \left[F_c(\dot\theta_1)\cos\theta_1 + F_c(\dot\theta_2)\cos\theta_2\right] \\
&\quad - \left[F_I(\ddot\theta_1)\sin\theta_1 + F_I(\ddot\theta_2)\sin\theta_2\right] \\
F_{cy} &= \oslash \\
F_{cz} &= -(N_{z1}-N_{z2}) \\
&= -K_d(\dot x)\left[\sin\theta_1\cos\theta_1 - \sin\theta_2\cos\theta_2\right] \\
&\quad + \left[F_c(\dot\theta_1)\sin\theta_1 - F_c(\dot\theta_2)\sin\theta_2\right] \\
&\quad - \left[F_I(\ddot\theta_1)\cos\theta_1 - F_I(\ddot\theta_2)\cos\theta_2\right]
\end{aligned} \tag{A.5}$$

$$\begin{aligned}
T_{cx} &= -a_c(N_{z1}+N_{z2}) \\
&= -a_c K_d(\dot x)\left[\sin\theta_1\cos\theta_1 + \sin\theta_2\cos\theta_2\right] \\
&\quad + a_c\left[F_c(\dot\theta_1)\sin\theta_1 + F_c(\dot\theta_2)\sin\theta_2\right] \\
&\quad - a_c\left[F_I(\ddot\theta_1)\cos\theta_1 + F_I(\ddot\theta_2)\cos\theta_2\right] \\
T_{cy} &= b_c(N_{z1}-N_{z2}) - (M_{y1}-M_{y2}) \\
&= -b_c K_d(\dot x)\left[\sin\theta_1\left(\cos\theta_1 + \frac{l_c}{b_c}\right) - \sin\theta_2\left(\cos\theta_2 + \frac{l_c}{b_c}\right)\right] \\
&\quad + b_c\left[F_c(\dot\theta_1)\sin\theta_1 - F_c(\dot\theta_2)\sin\theta_2\right] \\
&\quad - b_c\left[F_I(\ddot\theta_1)\left(\cos\theta_1 + \frac{l_c}{b_c}\right) - F_I(\ddot\theta_2)\left(\cos\theta_2 + \frac{l_c}{b_c}\right)\right] \\
&\quad - \left[T_I(\ddot\theta_1) - T_I(\ddot\theta_2)\right]
\end{aligned} \tag{A.6}$$

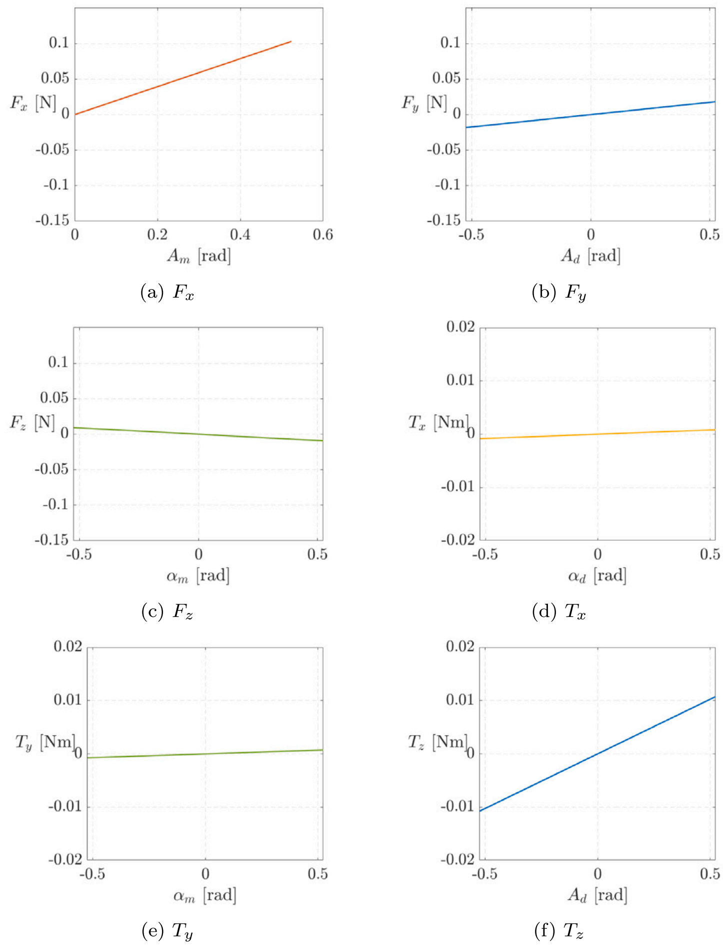

Fig. A.26. Relationship between control variables and forces applied on the system.

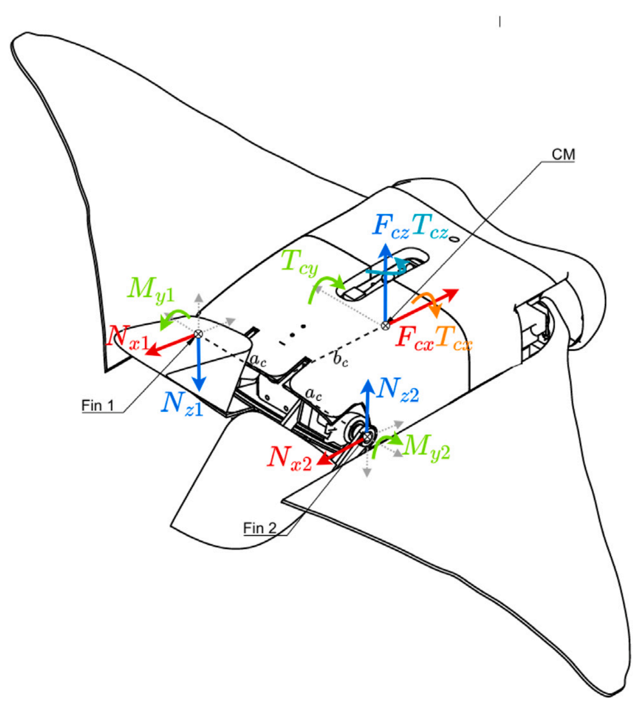

Fig. A.27. Equivalent forces and moments applied to the center of mass, generated by the caudal fin movement.

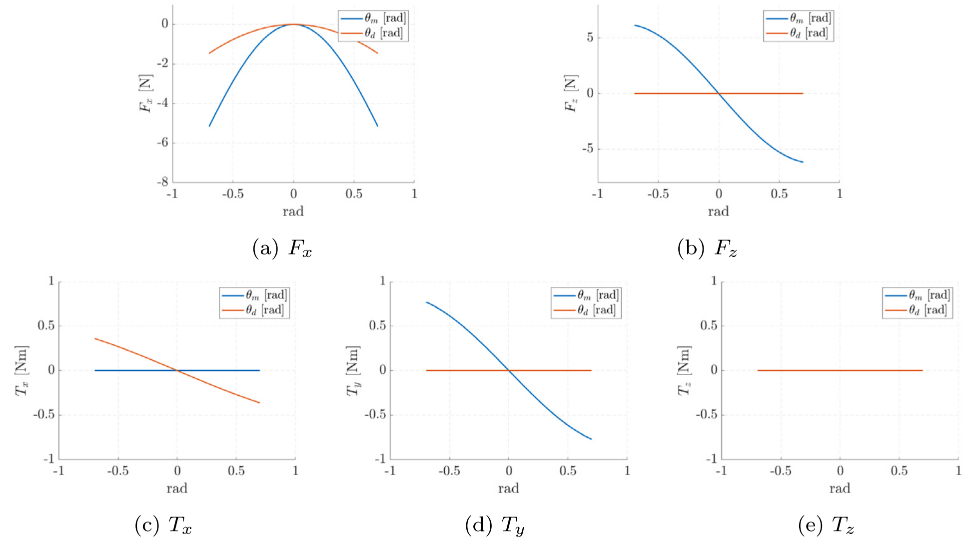

Fig. A.28. Relationship between θ_m (in blue) and θ_d (in red) and forces applied on the robot.

$$
\begin{aligned}
T_{cz} &= a_c(N_{x1} - N_{x2}) \\
&= K_d(\dot{x})\left[\sin^2\theta_1 - \sin^2\theta_2\right] \\
&\quad + \left[F_c(\dot{\theta}_1)\cos\theta_1 - F_c(\dot{\theta}_2)\cos\theta_2\right] \\
&\quad + \left[F_I(\ddot{\theta}_1)\sin\theta_1 - F_I(\ddot{\theta}_2)\sin\theta_2\right]
\end{aligned}
$$

A.6. Relationships between caudal kinematic variables and forces on the axis

See Fig. A.28.

Appendix B. Supplementary data

Supplementary material related to this article can be found online at https://doi.org/10.1016/j.oceaneng.2026.127077.

References

Asada, T., Tsujimoto, T., Oki, T., Furuhashi, H., 2025. Design and Control of Multi-Rigid Link Pectoral Fins Using Virtual Spring-Damper System for a Manta Ray Robot. IEEE Access 13, 78769–78780. http://dx.doi.org/10.1109/ACCESS.2025.3562081.

Bianchi, G., Cinquemani, S., 2022. Design of a Bioinspired Cownose Ray Robot. In: Martín-Palma, R.J., Knez, M., Lakhtakia, A. (Eds.), Bioinspiration, Biomimetics, and Bioreplication XII. 12041, International Society for Optics and Photonics,SPIE, p. 1204105. http://dx.doi.org/10.1117/12.2613115.

Bianchi, G., Cinquemani, S., Schito, P., Resta, F., 2021. A Numerical Model for the Analysis of the Locomotion of a Cownose Ray. J. Fluids Eng. 144, http://dx.doi.org/10.1115/1.4052048.

Bianchi, G., Maffi, L., Cinquemani, S., 2023a. Development of an underwater robot with undulation propulsion. In: Knez, M., Lakhtakia, A., Martín-Palma, R.J. (Eds.), Bioinspiration, Biomimetics, and Bioreplication XIII. 12481, International Society for Optics and Photonics,SPIE, p. 124810F. http://dx.doi.org/10.1117/12.2658708.

Bianchi, G., Maffi, L., Tealdi, M., Cinquemani, S., 2023b. A Bioinspired Cownose Ray Robot for Seabed Exploration. Biomimetics 8 (1), 30. http://dx.doi.org/10.3390/biomimetics8010030.

Bianchi, G., Maffi, L., Tealdi, M., Cinquemani, S., 2023c. Design and performance of a cownose ray-inspired robot for underwater exploration. In: Meder, F., Hunt, A., Margheri, L., Mura, A., Mazzolai, B. (Eds.), Biomimetic and Biohybrid Systems. Springer Nature Switzerland, Cham, pp. 244–265.

Cai, Y., Bi, S., Li, G., Hildre, H.P., Zhang, H., 2019. From Natural Complexity to Biomimetic Simplification: The Realization of Bionic Fish Inspired by the Cownose Ray. IEEE Robot. Autom. Mag. 26 (3), 27–38. http://dx.doi.org/10.1109/MRA.2018.2861985.

Cai, Y., Bi, S., Zhang, L., 2010. Design and implication of a bionic pectoral fin imitating cow-nosed ray. In: 2010 IEEE/RSJ International Conference on Intelligent Robots and Systems. IEEE, Taipei, pp. 3525–3529. http://dx.doi.org/10.1109/IROS.2010.5650804.

Cao, Y., Cao, Y., Ma, S., Li, X., Qu, Y., Cao, Y., 2023. Realization and online optimization for gliding and flapping propulsion of a manta ray robot. J. Mar. Sci. Eng. 11 (11), http://dx.doi.org/10.3390/jmse11112173, URL https://www.mdpi.com/2077-1312/11/11/2173.

Chen, L., Bi, S., Cai, Y., Cao, Y., Pan, G., 2022. Design and experimental research on a bionic robot fish with tri-dimensional soft pectoral fins inspired by cownose ray. J. Mar. Sci. Eng. 10 (4), http://dx.doi.org/10.3390/jmse10040537, URL https://www.mdpi.com/2077-1312/10/4/537.

Chew, C.-M., Lim, Q.-Y., Yeo, K.S., 2015. Development of propulsion mechanism for Robot Manta Ray. In: 2015 IEEE International Conference on Robotics and Biomimetics (ROBIO). pp. 1918–1923. http://dx.doi.org/10.1109/ROBIO.2015.7419053.

de Kruif, B., Cozijn, H., Schaaf, H., 2019. Control design for a multi-regime 6-DOF underwater vehicle; development of MARIN's modular AUV. IFAC-PapersOnLine 52, http://dx.doi.org/10.1016/j.ifacol.2019.12.312.

Fenco, L., Pérez-Zuñiga, G., Quiroz, D., Cuellar, F., 2021. Model Reference Adaptive Fuzzy Controller of a 6-DOF Autonomous Underwater Vehicle. In: OCEANS 2021: San Diego – Porto. pp. 1–7. http://dx.doi.org/10.23919/OCEANS44145.2021.9706083.

Fish, F., Schreiber, C., Moored, K., Liu, G., Dong, H., Bart-Smith, H., 2016. Hydrodynamic Performance of Aquatic Flapping: Efficiency of Underwater Flight in the Manta. Aerospace 3, 20. http://dx.doi.org/10.3390/aerospace3030020.

Fogh Sørensen, F., Mai, C., von Benzon, M., Liniger, J., Pedersen, S., 2025. The localization problem for underwater vehicles: An overview of operational solutions. Ocean Eng. 330, 121173. http://dx.doi.org/10.1016/j.oceaneng.2025.121173.

Garcia-Nava, S., García-Rangel, M.A., Zamora-Suárez, Á.E., Manzanilla-Magallanes, A., Muñoz, F., Lozano, R., Serrano-Almeida, A., 2023. Development of a 6 Degree of Freedom Unmanned Underwater Vehicle: Design, Construction and Real-Time Experiments. J. Mar. Sci. Eng. 11 (9), 1744. http://dx.doi.org/10.3390/jmse11091744.

Gołąbek, M., Welcer, M., Szczepański, C., Krawczyk, M., Zajdel, A., Borodacz, K., 2022. Quaternion Attitude Control System of Highly Maneuverable Aircraft. Electronics 11 (22), 3775. http://dx.doi.org/10.3390/electronics11223775, URL https://www.mdpi.com/2079-9292/11/22/3775.

Hao, Y., Cao, Y., Cao, Y., Huang, Q., Pan, G., 2022. Course Control of a Manta Robot Based on Amplitude and Phase Differences. J. Mar. Sci. Eng. 10 (2), 285. http://dx.doi.org/10.3390/jmse10020285.

He, J., Cao, Y., Qu, Y., Liu, X., Cao, Y., Dong, X., Yu, J., Pan, G., 2025. Development and experiment of manta ray-inspired robot actuated by dielectric elastomer actuator. IEEE Robot. Autom. Lett. 10 (10), 10466–10473. http://dx.doi.org/10.1109/LRA.2025.3586522.

He, Y., Xie, Y., Pan, G., Cao, Y., Huang, Q., Ma, S., Zhang, D., Cao, Y., 2022. Depth and Heading Control of a Manta Robot Based on S-Plane Control. J. Mar. Sci. Eng. 10 (11), 1698. http://dx.doi.org/10.3390/jmse10111698.

Hong, E.Y., Soon, H.G., Chitre, M., 2010-05. Depth control of an autonomous underwater vehicle, STARFISH. In: Oceans'10 IEEE Sydney. pp. 1–6. http://dx.doi.org/10.1109/OCEANSSYD.2010.5603566, URL https://ieeexplore.ieee.org/document/5603566.

Kokegei, M., He, F., Sammut, K., 2008. Fully coupled 6 degrees-of-freedom control of Autonomous Underwater Vehicles. In: Proceedings of MTS/IEEE OCEANS '08. IEEE, Quebec City, Canada, pp. 1–7. http://dx.doi.org/10.1109/OCEANS.2008.5152090.

Liu, A., Xing, C., Cao, W., Liu, B., Wang, S., Jin, J., Zhang, W., Li, K., Lu, Y., Hao, Y., Cao, Y., Cao, Y., 2025. Bio-inspired intermittent locomotion: A novel energy-saving strategy for manta ray-inspired underwater vehicles. Ocean Eng. 341, 122425. http://dx.doi.org/10.1016/j.oceaneng.2025.122425.

Low, K.H., Zhou, C., Seet, G., Bi, S., Cai, Y., 2011. Improvement and testing of a robotic manta ray (roman-III). In: 2011 IEEE International Conference on Robotics and Biomimetics. ROBIO, pp. 1730–1735. http://dx.doi.org/10.1109/ROBIO.2011.6181539.

Lu, Y., Meng, S., Xing, C., Hao, Y., Cao, Y., Pan, G., Cao, Y., 2024. Effect of Active–Passive Deformation on the Thrust by the Pectoral Fins of Bionic Manta Robot. J. Bionic Eng. 21 (2), 718–728. http://dx.doi.org/10.1007/s42235-023-00463-6.

Ma, H., Cai, Y., Wang, Y., Bi, S., Gong, Z., 2015. A biomimetic cownose ray robot fish with oscillating and chordwise twisting flexible pectoral fins. Ind. Robot.: Int. J. Robot. Res. Appl. 42 (3), 214–221. http://dx.doi.org/10.1108/IR-11-2014-0426, arXiv:https://www.emerald.com/ir/article-pdf/42/3/214/1197592/ir-11-2014-0426.pdf.

Macenski, S., Foote, T., Gerkey, B., Lalancette, C., Woodall, W., 2022. Robot Operating System 2: Design, Architecture, and Uses In The Wild. Sci. Robot. 7 (66), eabm6074. http://dx.doi.org/10.1126/scirobotics.abm6074, arXiv:2211.07752.

Macenski, S., Soragna, A., Carroll, M., Ge, Z., 2023. Impact of ROS 2 Node Composition in Robotic Systems. http://dx.doi.org/10.48550/arXiv.2305.09933, arXiv:2305.09933.

Madgwick, S., Harrison, A., Vaidyanathan, R., 2011. Estimation of IMU and MARG orientation using a gradient descent algorithm. IEEE Int. Conf. Rehabil. Robot. : [Proceedings] 2011, 5975346. http://dx.doi.org/10.1109/ICORR.2011.5975346.

Meng, Y., Wu, Z., Chen, D., Zhang, P., Tan, M., Yu, J., 2024. Development and 3-D Path-Following Control of an Agile Robotic Manta With Flexible Pectoral Fins. IEEE Trans. Cybern. 54 (6), 3727–3738. http://dx.doi.org/10.1109/TCYB.2023.3252589.

Picardi, G., Borrelli, C., Sarti, A., Chimienti, G., Calisti, M., 2020. A Minimal Metric for the Characterization of Acoustic Noise Emitted by Underwater Vehicles. Sensors (Basel, Switzerland) 20 (22), 6644. http://dx.doi.org/10.3390/s20226644, URL https://pmc.ncbi.nlm.nih.gov/articles/PMC7699715/.

Portugal, D., Rocha, R., Castilho, J., 2024. Inquiring the robot operating system community on the state of adoption of the ROS 2 robotics middleware. Int. J. Intell. Robot. Appl. 9, 454–479. http://dx.doi.org/10.1007/s41315-024-00393-4.

Railey, K., 2018. Demonstration of passive acoustic detection and tracking of unmanned underwater vehicles. http://dx.doi.org/10.1575/1912/10414.

Rosenberger, L., 2001. Pectoral Fin Locomotion in Batoid Fishes: Undulation Versus Oscillation. J. Exp. Biology 204, 379–394. http://dx.doi.org/10.1242/jeb.204.2.379.

Salazar, R., Fuentes, V., Abdelkefi, A., 2018. Classification of biological and bioinspired aquatic systems: A review. Ocean Eng. 148, 75–114. http://dx.doi.org/10.1016/j.oceaneng.2017.11.012, URL https://www.sciencedirect.com/science/article/pii/S0029801817306790.

Scudeletti, T., 2025. Maui. https://github.com/ScudeT/Maui,

Sfakiotakis, M., Lane, D.M., Davies, J.B.C., 1999. Review of fish swimming modes for aquatic locomotion. IEEE J. Ocean. Eng. 24 (2), 237–252. http://dx.doi.org/10.1109/48.757275, URL https://ieeexplore.ieee.org/document/757275.

Webb, P.W., 1988. Simple Physical Principles and Vertebrate Aquatic Locomotion. Amer. Zool. 28 (2), 709–725, URL https://www.jstor.org/stable/3883299.

Xing, C., Cao, Y., Cao, Y., Pan, G., Huang, Q., 2022. Asymmetrical oscillating morphology hydrodynamic performance of a novel bionic pectoral fin. J. Mar. Sci. Eng. 10 (2), http://dx.doi.org/10.3390/jmse10020289, URL https://www.mdpi.com/2077-1312/10/2/289.

Yuan, H., Kong, M., Wang, M., Cui, W., Pan, Y., Zhou, H., Yang, Q., 2024-04-22. Effect of turbulence-induced sediment resuspension and sedimentation on underwater wireless optical communication. Opt. Express 32 (9), 16292–16306. http://dx.doi.org/10.1364/OE.519243, arXiv:38859260.

Zhang, D., Pan, G., Cao, Y., Huang, Q., Cao, Y., 2022. A novel integrated gliding and flapping propulsion biomimetic manta-ray robot. J. Mar. Sci. Eng. 10 (7), http://dx.doi.org/10.3390/jmse10070924, URL https://www.mdpi.com/2077-1312/10/7/924.

Zhang, Y., Wang, S.-P., Wang, X., Geng, Y., 2018. Design and Control of Bionic Manta Ray Robot With Flexible Pectoral Fin. IEEE, p. 1039. http://dx.doi.org/10.1109/ICCA.2018.8444283.

Zhang, S., Xie, X., Sui, Y., Qu, Y., Zheng, G., Deng, Z., 2026. Dynamic modeling and stiffness optimization for a manta ray-inspired robot. Int. J. Mech. Sci. 316, 111417. http://dx.doi.org/10.1016/j.ijmecsci.2026.111417, URL https://www.sciencedirect.com/science/article/pii/S0020740326002730.